Dipole Response of Millennial Variability in Tropical South American Precipitation and $\delta^{18}O_p$ during the Last Deglaciation. Part I: Rainfall Response

YUNTAO BAO,[a] ZHENGYU LIU,[a] AND CHENGFEI HE[b]

[a] Department of Geography, The Ohio State University, Columbus, Ohio
[b] Rosenstiel School of Marine, Atmospheric, and Earth Science, University of Miami, Miami, Florida

(Manuscript received 12 March 2022, in final form 27 April 2023, accepted 28 April 2023)

ABSTRACT: Oxygen isotope speleothems have been widely used to infer past climate changes over tropical South America (TSA). However, the spatial patterns of the millennial precipitation and precipitation $\delta^{18}O$ ($\delta^{18}O_p$) response have remained controversial, and their response mechanisms are unclear. In particular, it is not clear whether the regional precipitation represents the intensity of the millennial South American summer monsoon (SASM). Here, we study the TSA hydroclimate variability during the last deglaciation (20–11 ka ago) by combining transient simulations of an isotope-enabled Community Earth System Model (iCESM) and the speleothem records over the lowland TSA. Our model reasonably simulates the deglacial evolution of hydroclimate variables and water isotopes over the TSA, albeit underestimating the amplitude of variability. North Atlantic meltwater discharge is the leading factor driving the TSA's millennial hydroclimate variability. The spatial pattern of both precipitation and $\delta^{18}O_p$ show a northwest–southeast dipole associated with the meridional migration of the intertropical convergence zone, instead of a continental-wide coherent change as inferred in many previous works on speleothem records. The dipole response is supported by multisource paleoclimate proxies. In response to increased meltwater forcing, the SASM weakened (characterized by a decreased low-level easterly wind) and consequently reduced rainfall in the western Amazon and increased rainfall in eastern Brazil. A similar dipole response is also generated by insolation, ice sheets, and greenhouse gases, suggesting an inherent stability of the spatial characteristics of the SASM regardless of the external forcing and time scales. Finally, we discuss the potential reasons for the model–proxy discrepancy and pose the necessity to build more paleoclimate proxy data in central-western Amazon.

SIGNIFICANCE STATEMENT: We want to reconcile the controversy on whether there is a coherent or heterogeneous response in millennial hydroclimate over tropical South America and to clearly understand the forcing mechanisms behind it. Our isotope-enabled transient simulations fill the gap in speleothem reconstructions to capture a complete picture of millennial precipitation/$\delta^{18}O_p$ and monsoon intensity change. We highlight a heterogeneous dipole response in precipitation and $\delta^{18}O_p$ on millennial and orbital time scales. Increased meltwater discharge shifts ITCZ southward and favors a wet condition in coastal Brazil. Meanwhile, the low-level easterly and the summer monsoon intensity reduced, causing a dry condition in the central-western Amazon. However, the millennial variability of hydroclimate response is underestimated in our model, together with the lack of direct paleoclimate proxies in the central-west Amazon, complicating the interpretation of changes in specific paleoclimate events and posing a challenge to constraining the spatial range of the dipole. Therefore, we emphasize the necessity to increase the source of proxies, enhance proxy interpretations, and improve climate model performance in the future.

KEYWORDS: South America; Monsoons; Climate variability; Paleoclimate

1. Introduction

Hydroclimate variability over tropical South America (TSA) is largely influenced by the South American summer monsoon (SASM) system (Zhou and Lau 1998) and is of great importance for ecosystem evolution there (Mayle et al. 2000; Fornace et al. 2016). Thus, it is important to improve our understanding of the long-term response of SASM to climate change. One controversial issue on SASM is whether the precipitation and $\delta^{18}O_p$ exhibit a dipole response in millennial variability. During the Heinrich Stadial 1 (HS1), existing speleothem records tend to show a depletion in $\delta^{18}O_p$ across eastern Brazil from the north (Stríkis et al. 2018; Cruz et al. 2009) to the south (Wang et al. 2007; Novello et al. 2017), along with a site in the northwestern corner of Amazon (Mosblech et al. 2012), implying increased rainfall if the amount effect is dominant. Taking these records as a coherent $\delta^{18}O_p$ signal across the TSA region, Cheng et al. (2013) and Novello et al. (2017) suggest a picture that SASM exhibits a coherent pattern of millennial variability across the TSA region. In particular, at HS1, the TSA region experiences an increased SASM intensity with a coherent wet condition across the TSA region (Burckel et al. 2015; Stríkis et al. 2018), which is caused by the increased

---

Denotes content that is immediately available upon publication as open access.

Supplemental information related to this paper is available at the Journals Online website: https://doi.org/10.1175/JCLI-D-22-0172.s1.

Corresponding authors: Yuntao Bao, bao.291@osu.edu; Zhengyu Liu, liu.7022@osu.edu

DOI: 10.1175/JCLI-D-22-0172.1

freshwater discharge over North Atlantic basin, the weakened Atlantic meridional overturning circulation (AMOC), the southward migration of the intertropical convergence zone (ITCZ) (Kanner et al. 2012; Stríkis et al. 2015; Wang et al. 2017) and, finally, the intensified South Atlantic convergence zone (SACZ) (Kanner et al. 2012; Stríkis et al. 2015; Wang et al. 2017).

This widely accepted picture of a coherent millennial change of SASM rainfall across the TSA region, however, remains controversial. First, multisource proxies tend to show a dipole response in moisture conditions. Paleoclimate proxies such as stabilized fluvial and eolian sediment records from the northern Amazon (Zular et al. 2019) and offshore marine sediment records to the north of TSA (Campos et al. 2019) suggest a significant drying at HS1. In contrast, eastern Brazil speleothem and offshore marine sediment records (Campos et al. 2019) suggest a wet condition at HS1. Therefore, combining all kinds of paleoclimate proxies, a northwest–southeast dipole in precipitation change can be seen for millennial variability, with decreased precipitation over the central-western Amazon, increased precipitation over eastern Brazil, and little precipitation change in subtropical continent. The heterogeneous spatial pattern in millennial precipitation variability seems consistent with coupled climate model simulations (Mohtadi et al. 2016; Campos et al. 2019) and idealized meltwater hosing experiments at the Last Glacial Maximum (Jackson et al. 2015). Second, at precessional or orbital time scale, speleothem δ^{18}O records over the TSA region shows a heterogeneous dipole response associated with austral summer insolation, with the δ^{18}O out of phase between western Amazon–southern razil and eastern–northeastern Brazil (Cruz et al. 2009; Cheng et al. 2013). This dipole response is further supported by snapshot simulations in isotope-enabled climate models (Cruz et al. 2009; Liu and Battisti 2015). Low austral summer insolation leads to cooling over the South American continent and thus decreases easterly monsoon wind and western Amazon precipitation. In contrast, northern Africa cooling produces a strengthened African winter monsoon and then a southward shift of the Atlantic ITCZ, increasing precipitation in eastern Brazil (Liu and Battisti 2015).

The above discussion also brings up an important point on SASM: it may not be proper to infer the intensity of SASM in a single rainfall index if the rainfall responses and corresponding large-scale atmospheric circulation (or SASM system) are not coherent across the TSA region. A useful analogy can be seen over East Asia, where East Asia summer monsoon (EASM) rainfall response exhibits a north–south dipole at millennial and precessional time scales because the EASM system migrates meridionally with the low-level southerly monsoon wind and upper-level westerly jet (Liu et al. 2014; He et al. 2021a). Given the potential inhomogeneity of the SASM rainfall response, the available speleothem records may not capture the complete picture of δ^{18}O/precipitation change on millennial time scales and may not be enough to infer the change of SASM system intensity, because most available speleothem records for inferring millennial variability are located over the Andes and eastern Brazil regions, with few in the interior Amazon basin. As such, the widely accepted notion that a strengthened SASM responds to increased meltwater forcing (Kanner et al. 2012; Cheng et al. 2013; Stríkis et al. 2015; Novello et al. 2017; Stríkis et al. 2018) deserves further investigation.

Here we address the question of whether there is a robust continental-scale dipole in both orbital and millennial precipitation and $\delta^{18}O_p$ over the TSA, with a special focus on the millennial time scale. If so, what mechanisms induce such a large-scale dipole response of the millennial hydroclimate variability? A further question is: what is a proper index for the SASM intensity if it is considered as an entity varying at millennial time scales? How does SASM respond to meltwater forcing? Previous modeling studies on the SASM response to meltwater forcing have employed the highly idealized snapshot hosing experiments without $\delta^{18}O_p$. Here, we will study the evolution of SASM and the accompanying δ^{18}O in the last deglaciation by analyzing a set of transient simulations in an isotope-enabled Earth system model during the last deglaciation (He et al. 2021a). We show that the millennial variability of SASM is characterized by a northwestern–southeastern dipole response in both rainfall and $\delta^{18}O_p$, with opposite changes between the central-western Amazon and eastern Brazil. The dipole response is caused primarily by meltwater-driven atmospheric circulation anomalies. We argue that in response to meltwater forcing, the SASM intensity reduced, which is characterized by a decreased low-level easterly wind, decreased precipitation (increased $\delta^{18}O_p$) in the central-western Amazon, and increased precipitation (decreased $\delta^{18}O_p$) in eastern Brazil. We note that reconstructed $\delta^{18}O_p$ (or precipitation in the sense of amount effect) over eastern Brazil itself is not a proper indicator of the SASM intensity due to the limited spatial coverage of speleothem records. In this paper, we will focus on mechanisms that drive the dipole rainfall response, with the mechanism for the dipole $\delta^{18}O_p$ response to be presented in a follow-up article (Bao et al. 2023). Note that the dipole is collectively referred to as the "northwestern–southeastern dipole" in this study for simplification, which includes all expressions, such as "east–west dipole" or "north–south dipole" in previous studies in both millennial and orbital time scales.

2. Methods

a. The model

We use the state-of-the-art Community Earth System Model, version 1.3, with fully coupled water isotope modules (iCESM) in the atmosphere, ocean, land, sea ice, and river runoff components (Brady et al. 2019). The atmosphere component is the Community Atmosphere Model (CAM5.3) (Neale et al. 2010) and is on a 2.5° longitude × 1.9° latitude finite-volume grid with 30 hybrid vertical levels. The land component is the Community Land Model (CLM4) (Oleson et al. 2010), with the same horizontal grid as the atmosphere and 10 vertical soil levels. The ocean component is the Parallel Ocean Program (POP2) (Smith et al. 2010), and the sea ice component is Los Alamos Sea Ice Model (CECE4) (Hunke 2010) with nominal 1° displaced-pole grids and 60 vertical levels. The iCESM well simulates the preindustrial and present-day climate (Hurrell et al. 2013). Besides, iCESM successfully captures the general observed features of precipitation isotope in the present climate (Brady et al. 2019; Nusbaumer et al. 2017) and past climate over the high-latitude and Asian monsoon regions (He et al. 2021a,b).

b. *iTRACE simulations*

Using iCESM, we conducted a series of transient climate simulations [the all-forcing isotope-enabled transient climate experiment (iTRACE)] of the evolution of climate variables and water isotopes (δ^{18}O and δD) during the last deglaciation (20–11 Ka before present) (He et al. 2021a). The iTRACE simulations follow a similar model strategy to the previous transient simulation TRACE-21 ka (Liu et al. 2009). More details on iTRACE techniques are described in He et al. (2021a). Our transient simulations incorporate water isotopes, making it feasible for a direct model–proxy data comparison on δ^{18}O and a comprehensive analysis of hydroclimate variability over the TSA region. iTRACE has been shown to reproduce the deglacial variability of $\delta^{18}O_p$ in good agreement with the speleothem records across the pan-Asian monsoon region (He et al. 2021a) as well as over Greenland (He et al. 2021b) and Antarctica (Buizert et al. 2021).

Our transient simulations include four sensitivity experiments that are forced by four forcing factors (ice sheet, solar insolation, greenhouse gases, and meltwater flux) applied additively. The first sensitivity experiment is driven by ice sheet volume and ocean bathymetry (ICE), starting from the Last Glacial Maximum (LGM; 20 ka). Insolation forcing with changing orbital parameters is then added (ICE+ORB) for the second sensitivity experiment. Followed by is the third sensitivity experiment, driven by additive greenhouse gases (GHG), including CO_2, CH_4, and N_2O (ICE+ORB+GHG). Meltwater flux (ICE+ORB+GHG+MWF) is then added for the last sensitivity experiment, namely, iTRACE. The additive sensitivity experiments allow us to isolate each forcing effect, including the ice sheet effect, the orbital effect, the greenhouse gases effect, and the meltwater effect. Note that this is an approximate way of decomposing the effect of each forcing factor assuming a linear effect, although there may be nonlinearity effect in between.

We note that model bias from tropical sea surface temperature (SST) (not shown) may compromise accuracy in simulated precipitation over the TSA. To test whether the SST bias may affect the results and arguments, we perform a set of atmospheric-only snapshot simulations prescribed by the corrected model SST for the preindustrial (PI), LGM, and HS1 periods. All simulations are integrated for 40 years, with the last 20 years used for analysis. Technically, we first take the difference between observational and coupled model SST in the PI period to get the model SST bias (only for tropical and subtropical regions 40°S–40°N). Then, the diagnosed SST bias is added to the original coupled model SST to get the "corrected" SST prescribed in LGM and HS1 simulation. As such, the effect of tropical SST bias on simulated precipitation and $\delta^{18}O_p$ can be removed.

c. *Model $\delta^{18}O_c$*

To compare our model with the records reconstructed from speleothems, we derive the model $\delta^{18}O_c$ from $\delta^{18}O_p$ with the same method as He et al. (2021a). Here, calcite δ^{18}O ($\delta^{18}O_c$) in speleothems differs from precipitation $\delta^{18}O_p$ due to the dependency on cave temperature. First, the unit of precipitation $\delta^{18}O_{p\text{-SMOW}}$ is converted to water $\delta^{18}O_{W\text{-PDB}}$ (Coplen et al. 1983):

$$\delta^{18}O_{W-\mathrm{PDB}} = 0.970\,02 \times \delta^{18}O_{p-\mathrm{SMOW}} - 29.98. \tag{1}$$

Then $\delta^{18}O_c$ is derived from the temperature-dependent equilibrium equation of inorganic carbonate oxygen isotope (O'Neil et al. 1989):

$$\delta^{18}O_c = \delta^{18}O_{W-\mathrm{PDB}} + 2.70 \times 10^6/T^2 - 3.29, \tag{2}$$

where T is the absolute cave temperature (in K). We use the model annual mean surface temperature as an analog to cave temperature.

The temperature contribution to $\delta^{18}O_c$ can be roughly estimated from the first-order approximation of Eq. (2):

$$\delta^{18}O'_c = \delta^{18}O'_{W-\mathrm{PDB}} - 5.4 \times 10^6 \frac{T'}{\overline{T}^3}. \tag{3}$$

Given $\overline{T} \sim 290$ K, the deglacial temperature sensitivity to the difference between $\delta^{18}O_c$ and $\delta^{18}O_p$ is $-5.4 \times 10^6(1/\overline{T}^3) = -0.22‰\ \mathrm{K}^{-1}$. For the millennial time scale (HS1 relative to LGM, for example), the average 1.5°C model surface temperature increase at TSA speleothem sites induces 0.31‰ depletion in $\delta^{18}O_c$, which accounts for ~22% of the total $\delta^{18}O_c$ depletion (1.4‰) at HS1. For the orbital time scale (when comparing 11 ka before present and LGM), the average 4°C model surface temperature over the TSA induces 0.84‰ depletion in $\delta^{18}O_c$, which account for ~58% of the total $\delta^{18}O_c$ depletion (1.45‰). This indicates that the effect of temperature on $\delta^{18}O_c$ value is important in the orbital time scale but is less important for the millennial time scale over the TSA. Therefore, except for the model–proxy data comparison, for simplicity, we will mainly use $\delta^{18}O_p$ for further analysis of large-scale mechanisms in the following text so that the temperature-induced subprocesses in caves are excluded. As we suggested, this is feasible for the millennial time scale but not for the orbital time scale. As such, we will also perform the same analysis again for $\delta^{18}O_c$ and discuss the results that are different from $\delta^{18}O_p$.

d. *Variance contribution*

Since the four additive sensitivity experiments allow us to isolate each forcing effect (the ice sheet, the orbital, the GHG, and the meltwater effect), the variance contribution of each forcing factor to total iTRACE simulation can be estimated as follows:

$$y = \sum_{i=1}^{4} x_i + \varepsilon. \tag{4}$$

where y denotes a hydroclimate variable (either surface temperature, precipitation, or $\delta^{18}O_p$) in the iTRACE simulation during the last deglaciation, and x_i denotes the hydroclimate

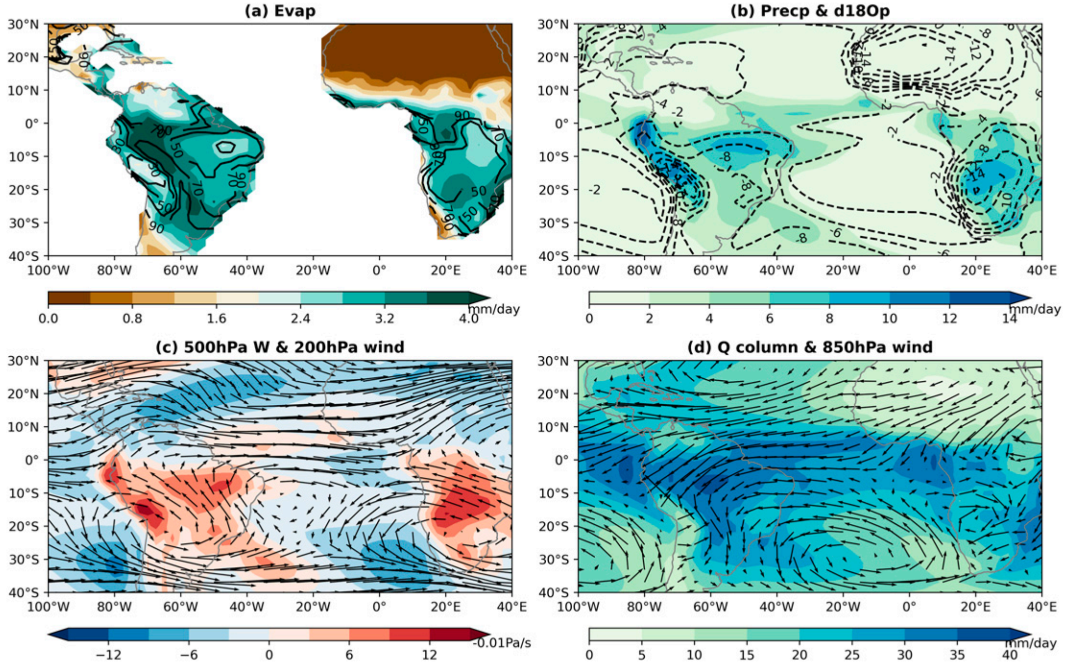

FIG. 1. iTRACE hydroclimate climatology at the LGM in DJF. (a) evapotranspiration (shading; in mm day^{-1}) and percentage ratio between evapotranspiration and precipitation (contours; in %); (b) precipitation (shading; in mm day^{-1}) and $\delta^{18}O_p$ (contours; in ‰; interval is 2‰ mil^{-1}); (c) 200 hPa wind (vectors; in 5 m s^{-1}) and 500 hPa vertical velocity (shading; in −0.01 Pa s^{-1}); (d) 850 hPa wind (vectors; in 3 m s^{-1}) and precipitable water (shading; in mm day^{-1}).

variable responding to each forcing factor during the last deglaciation. ε is the nonlinear interaction among each forcing. In our case, the effects of four forcing factors are largely independent ($\varepsilon \approx 0$) since the sum of the sensitivity experiments can largely reproduce the variability in the iTRACE simulation. Thus, the total variance of a variable in iTRACE simulation can be decomposed as follows (Fields 2003):

$$\mathrm{Cov}\left(\sum_{i=1}^{4} x_i,\, y\right) = \sum_{i=1}^{4} \mathrm{Cov}(x_i,\, y), \qquad \mathrm{Var}(y) = \sum_{i=1}^{4} \mathrm{Cov}(x_i,\, y). \tag{5}$$

Based on Eq. (5), the relative contribution of each forcing factor i to a variable of the iTRACE simulation can be obtained from Eq. (6):

$$R_i^2(y) = \frac{\mathrm{Cov}(x_i,\, y)}{\mathrm{Var}(y)}. \tag{6}$$

3. Model climatology

As a background, we first discuss the model climatology during the LGM as an example. The climatology in austral summer [December–February (DJF)] shows heavy rainfall rates and depleted $\delta^{18}O_p$ values in the northeastern and northwestern TSA regions (Fig. 1b), which are caused by the seasonal meridional shift of ITCZ into the Southern Hemisphere, corresponding to the shift of ascending branch of Hadley circulation. The high precipitation/depleted $\delta^{18}O_p$ region also extends southward (Fig. 1b) due to deep convection and ascending motion (Fig. 1c) over the SACZ region. In the upper troposphere, the SASM system is associated with the anticyclonic system of Bolivian high, centered at 22°S, 70°W (Fig. 1c), and Nordeste low, centered at eastern coastal Brazil (Fig. 1c). The Bolivian high produces ascent over the central-western Amazon, while Nordeste low produces subsidence over northeastern Brazil. In the lower level, the SASM system consists of the easterly monsoon wind associated with the South Atlantic Subtropical high, which transports moisture from the tropical South Atlantic into the South American continent, providing precipitable water there (Fig. 1d). Precipitation in northeastern Brazil and the Andes are mainly produced by upstream moisture transportation and convergence (Cook 2009), associated with low evapotranspiration and a relatively small ratio of evapotranspiration over precipitation (30%–40%) (Fig. 1a). In contrast, precipitation in the central-western Amazon is sensitive to local land–air interaction, characterized by a large ratio of evapotranspiration over precipitation (over 70%) (Fig. 1a).

Our model performance is validated through a comparison of the seasonal cycle between our PI simulation and the observations in five Global Network of Isotopes in Precipitation stations (GNIP; shown in purple stars in Fig. 3h1) over the TSA region (Fig. 2). The seasonal cycle patterns of model surface temperature agree with GNIP observations for the TSA, with a clear semiannual cycle in the deep tropics in western and central-western Amazon [Figs. 2a(1),a(2)] and a dominant annual cycle over eastern Brazil [Figs. 2a(3)–a(5)].

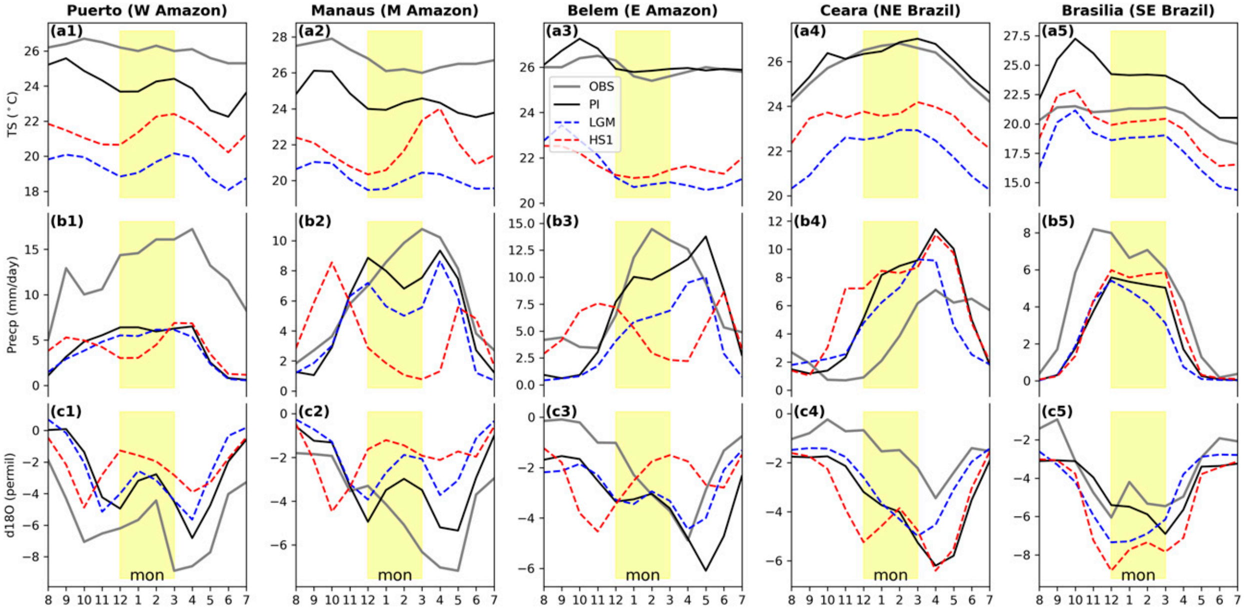

FIG. 2. Seasonal cycle of (top)surface temperature, (middle) precipitation, and (bottom) δ^{18}O for GNIP sites in the tropical South America: [a(1)],[b(1)],[c(1)] Puerto; [a(2)],[b(2)],[c(2)] Manaus; [a(3)],[b(3)],[c(3)] Belem; [a(4)],[b(4)],[c(4)] Ceara; [a(5)],[b(5)],[c(5)] Brasilia. Gray solid lines are for ERA5 climatology from 1979 to 2019; solid black lines are for model preindustrial climatology; blue and red dashed lines are for model LGM and HS1 climatology, respectively. Yellow shading indicates the warm and wet season of tropical South America.

Model precipitation shows a dominant annual cycle with the rainy season in the austral summer half-year (November–March), as in the observation across eastern Brazil [Figs. 2b(3)–b(5)], albeit the model maximum precipitation month in Belem shifts toward austral autumn. Model $\delta^{18}O_p$ also agrees with the observation in eastern Brazil, dominated by an annual cycle with the maximum depletion around April [Figs. 2c(3)–c(5)]. The δ^{18}O is roughly out of phase with rainfall in the sense of amount effect. This opposite δ^{18}O–precipitation correlation is also largely valid in western Amazon as in the observation, although the δ^{18}O also exhibits a significant semiannual variability that is not clearly present in precipitation [Fig. 2c(1)]. In contrast to other sites, in central Amazon on Manaus station [Figs. 2b(2),c(2)], precipitation ($\delta^{18}O_p$) exhibits an annual cycle with the maximum (minimum) around March (April) in the observation [as in eastern Brazil, Figs. 2c(3)–c(5)], but is dominated by a semiannual cycle in the model [Figs. 2b(2),c(2)]. We speculate that this model–observation inconsistency is caused by the model bias near the equatorial region, and Manaus is the closest GNIP site to the equator. One common bias in iCESM, as in most state-of-the-art models, is the tropical bias known as the precipitation "double ITCZ" bias (Lin 2007). As a result, the model ITCZ in the Amazon region shifts excessively southward (~7°S) compared to observation (~2°S) (not shown), causing an erroneous dry period in austral summer in the model [December–February; Figs. 2b(2),c(2)] when the model ITCZ crosses the latitude of Manaus (in November) to move farther southward. Therefore, except in central Amazon, our model seems to be able to capture the major features of the seasonal cycle of $\delta^{18}O_p$ in South America, dominated by the amount effect.

4. Model–data comparison on deglacial hydroclimate change

a. Direct comparison on deglacial $\delta^{18}O$ evolution

Our model $\delta^{18}O_c$ reproduces the overall pattern of the observed deglacial variability over most sites in the lowland TSA region (excluding the Andes here because of the relative low topography due to coarse model resolution), albeit with more depleted $\delta^{18}O_c$ values and underestimated amplitude of millennial variability compared to speleothems. Cave sites in the lowland TSA are concentrated in eastern Brazil, except for one (Paraíso) in the northern Amazon [Fig. 3h(1)]. The speleothem $\delta^{18}O_c$ records over eastern Brazil show a generally coherent millennial variability during the last deglaciation [Figs. 3b(2)–f(2)], characterized by a depletion during HS1 and the subsequent enrichment in Bølling–Allerød interstadial (BA), and depletion again in Younger Dryas stadial (YD), consistent with previous observations (Novello et al. 2017; Deininger et al. 2019). Our model $\delta^{18}O_c$, in general, is able to simulate the coherent millennial variability in speleothem $\delta^{18}O_c$ over eastern Brazil, but the values are more depleted [Figs. 3b(2)–f(2), note different scales between the model and observation]. When the proxy and model are constrained to the same scale (Fig. S1 in the supplemental material), we find that the amplitude of the millennial variability of the model $\delta^{18}O_c$ is well represented in Paixão. However, the model underestimates the amplitude of the $\delta^{18}O_c$ variability in Rio Grande, Lapa Sem Fim, Jaraguá, and Botuvera. Thus, four out of six cave sites of model $\delta^{18}O_c$ variability are underestimated. This is in contrast to the pan-Asian monsoon region (He et al. 2021a) and over Greenland (He et al. 2021b), where model

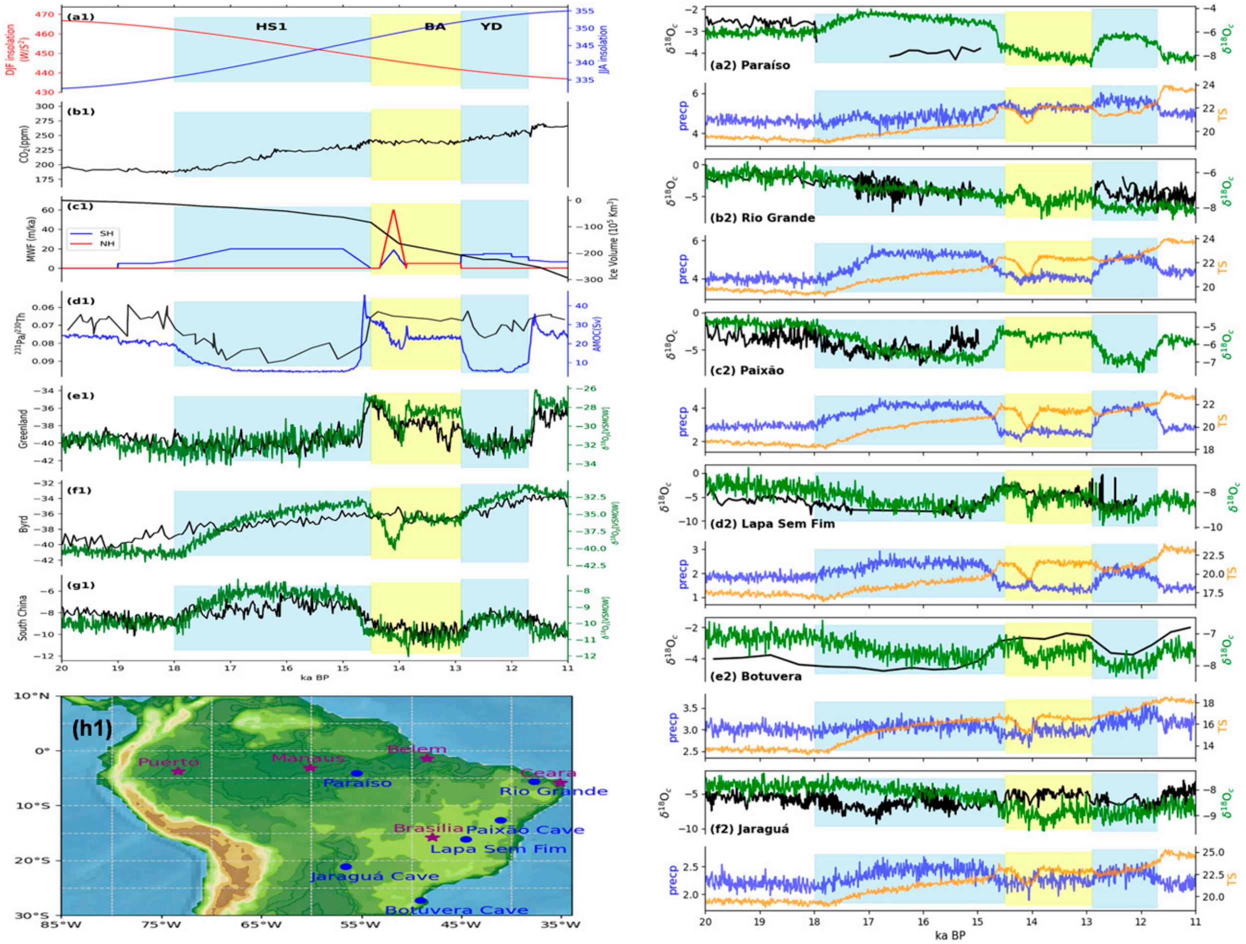

FIG. 3. Hydroclimate and δ^{18}O evolution in iTRACE and reconstructed proxy during the last deglaciation. [a(1)] Insolation forcing (w m^{-2}) at 15°S in DJF (red) and JJA (blue); [b(1)] Global mean atmospheric CO_2 concentration (ppm); [c(1)] meltwater fluxes (m Ka^{-1}) in the Northern (red; left axis) and Southern (blue; left axis) Hemisphere; global ice volume change (10^5 km^3) relative to LGM (black; right axis; Argus et al. 2014; Peltier et al. 2015); [d(1)] ^{231}Pa/$^{230\mathrm{Th}}$ reconstructed from sediment core GGC5 as a proxy for AMOC intensity (black) and model AMOC intensity (blue); [e(1)] Greenland (GISP2) ice-core $\delta^{18}O_p$ (black) and model annual mean $\delta^{18}O_p$ (green); [f(1)] ice-core $\delta^{18}O_p$ reconstructed from Antarctic Byrd (black) and model annual mean $\delta^{18}O_p$ (green); [g(1)] southern China speleothem proxy $\delta^{18}O_c$ (black; left axis) and model annual mean $\delta^{18}O_c$ (green; right axis); [h(1)] location of cave speleothem proxy (blue dots) and GNIP sites (purple stars) in tropical South America. Time series of speleothem proxy $\delta^{18}O_c$ (black; left axis) and model annual mean $\delta^{18}O_c$ (green; right axis), model annual mean precipitation (blue; left axis), and surface temperature (orange; right axis) in tropical South America: [a(2)] Paraíso (Wang et al. 2017); [b(2)] Rio Grande (Cruz et al. 2009); [c(2)] Paixão (Stríkis et al. 2018); [d(2)] Lapa Sem Fim (Stríkis et al. 2018), [e(2)] Botuvera (Wang et al. 2007), and [f(2)] Jaraguá (Novello et al. 2017). Note that model $\delta^{18}O_p$ and $\delta^{18}O_c$ are weighted by precipitation.

$\delta^{18}O_c$ agree well with observations in both the millennial variability pattern and magnitude [Figs. 3e(1),f(1),g(1)]. However, we note a similar problem occurred in other paleoclimate modeling studies: the centennial scale hydroclimate changes in South America over the last millennial are also underestimated in iCESM model (Orrison et al. 2022), and the response of eastern China $\delta^{18}O_p$ to orbital forcing in ECHAM model tends to be weaker than speleothem proxies (Battisti et al. 2014). The discrepancy between the model and proxy $\delta^{18}O_c$ indicates some dynamics or physics processes may not be captured by the model when focusing on specific paleoclimate events. The reason for the different magnitude of responses is briefly discussed in section 6 but still remains to be explored in the future. Nevertheless, the consistent millennial variability pattern and deglacial trend of $\delta^{18}O_c$ between the model and eastern Brazil speleothems makes our simulation a qualitatively useful surrogate to study the cause of the millennial variability because basic dynamics, at least, are captured by our model. In contrast, for the equatorial Amazon region, the model $\delta^{18}O_c$ millennial variability (HS1 relative to LGM) is inconsistent with the only speleothem cave record Paraíso [Fig. 3a(2)]: the former shows a slight enrichment in $\delta^{18}O_c$ from LGM into HS1, while the latter shows a substantial depletion. This model–data discrepancy of $\delta^{18}O_c$ over cave Paraíso (geographically close to Manaus and the equator) is likely due to the tropical “double ITCZ” bias in our model, as

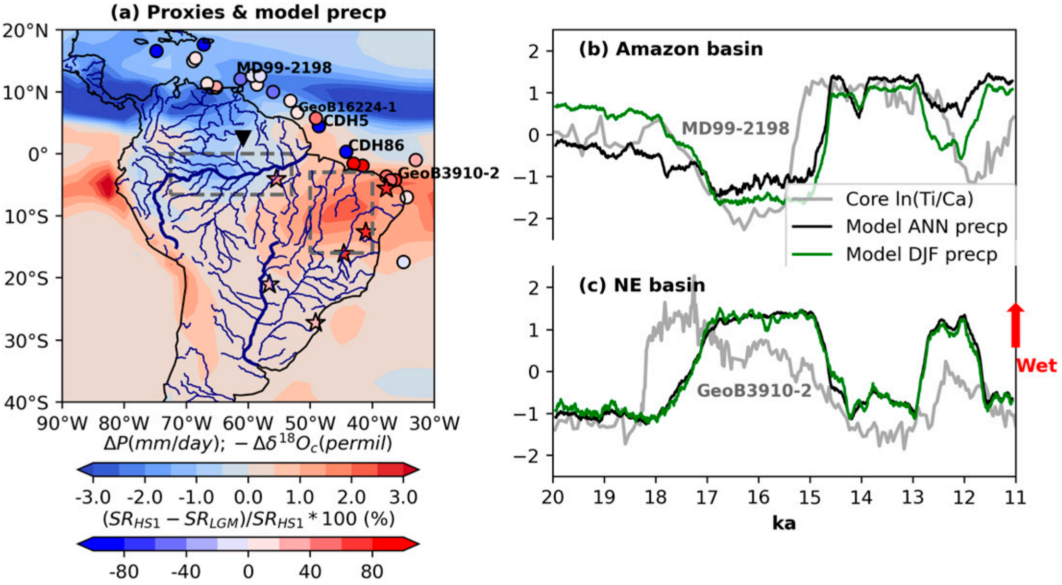

FIG. 4. iTRACE model and multisource paleoclimate proxies representing deglacial precipitation change in tropical south America: (a) Millennial response of annual mean precipitation change (HS1 − LGM) in iTRACE model (shading; in mm day^{-1}). Relative sediment rate (in %) change {[($SR_{HS1} - SR_{LGM}$)/SR_{HS1}] × 100%} that are derived from ocean sediment records (Zhang et al. 2015) along the north South American continental slope (blue dots mean decreased relative sediment rate at HS1 and likely linked to decreased rainfall and fluvial processes in the north Amazon, including Amazon River and Orinoco River drainage basins; red dots indicate increased relative sediment rate at HS1 and likely due to increased rainfall and fluvial processes in northeastern Brazil, mostly the Parnaíba River drainage basins). A stabilized fluvial and eolian land sediment record from Roraima (blue triangle), the northern Amazon, suggests decreased rainfall in northern Amazon in HS1 (Zular et al. 2019). Also shown are $\delta^{18}O_c$ difference between HS1 and LGM from available speleothem sites (asterisks; in ‰; see Fig. 3 for detail). To be consistent, we add a minus sign ($-\Delta\delta^{18}O_c$) so that the positive value indicates increased precipitation in the scenes of "amount effect." (b) Time series of ln(Ti/Ca) (gray line) derived from ocean sediment core MD99-2198 (Zhuravleva et al. 2021), overlaid with iTRACE model precipitation (black line for annual mean; green line for DJF) in Amazon River drainage basin [the area is shown in a dashed gray frame in (a)]. (c) Time series of ln(Ti/Ca) (gray line) derived from ocean sediment core GeoB3910-2 (Jaeschke et al. 2007), overlaid with iTRACE model precipitation (black line for annual mean; green line for DJF) in northeastern Brazil basin [the area is shown in dashed gray frame in (a)]. Note that all the time series in (b) and (c) are standardized and moving averaged by 200 years for comparison.

discussed previously (more discussions will be found in section 6). The seasonal evolution of model annual $\delta^{18}O_c$ shows that the millennial variability is contributed predominantly by DJF over most sites (Fig. S1), which corresponds to the mature phase of SASM with strong convection and high precipitation (Fig. 2). Along with the evolution of $\delta^{18}O$, model rainfall tends to also exhibit a coherent evolution across the eastern TSA sites. The deglacial evolution of rainfall is dominated by millennial variability, with increased rainfall in HS1, reduced rainfall in BA, and increased rainfall again in YD. This rainfall variability tends to be negatively correlated with the $\delta^{18}O$ changes, most clearly in Paixão and Lapa Sem Fim over the entire deglacial period [Figs. 3b(2)–f(2)]. The rainfall and $\delta^{18}O$ changes appear to be consistent with the isotopic "amount effect" for the eastern Brazil region, as suggested previously (Dansgaard 1964; Vuille et al. 2003a; Cruz et al. 2005). In contrast to precipitation, the model annual surface temperature is dominated by a coherent warming trend, which is possibly driven by the increased CO_2 concentration and reduced ice sheet volume [Figs. 3b(1),c(1)], as well as a small decrease in annual mean insolation associated with an increased obliquity (not shown).

b. Multiproxies and model comparison

Available $\delta^{18}O_c$ records reconstructed from lowland speleothem caves are limited in their spatial coverage to eastern Brazil and, therefore, cannot suggest long-term hydroclimate information in the vast Amazon region. In contrast, the climate model provides hydroclimate variables with complete spatial coverage, which requires multisource of paleoclimate proxy data to constrain the model performance. Taking the difference between HS1 and LGM as an analogy to millennial response, our model shows a "dipole response" in annual mean (ANN) precipitation (shading in Fig. 4a), with a contrasting change between eastern Brazil and the inland Amazon. Increased precipitation at HS1 in eastern Brazil is, again, supported by $\delta^{18}O_c$ from speleothem caves (asterisks in Fig. 4a) in the sense of "amount effect" (see section 4a). The increased precipitation is also supported by ocean sediments at the northeastern South American continental slope: increased relative sediment rate during HS1 (dots in Fig. 4a), and increased ln(Ti/Ca) of core GeoB3910-2 (Jaeschke et al. 2007) during HS1 and YD (gray line in Fig. 4c) reflects strengthened hydrological or fluvial processes in northeastern Brazil (mostly the Parnaíba River drainage basins) (Zhang et al. 2015). In contrast, evidence of decreased HS1 precipitation in the inland Amazon basin comes indirectly from sediment proxies: a fluvial and eolian land sediment record from the Roraima in the northern Amazon (triangle in Fig. 4a) documents the formation of the eolian dunes from LGM to HS1 (Zular et al. 2019), supporting a dry period. Additional evidence is provided by the ocean sediment cores at the northern South American continental slope: most cores document a reduced HS1 sediment rate (dots in Fig. 4a) and a decrease in ln(Ti/Ca) from core MD99-2198 (Zhuravleva et al. 2021) during HS1 and YD (gray line in Fig. 4b). This indicates a reduced fluvial process and deposition of fine-grain material in northeastern Brazil (mainly in the Amazon River and Orinoco River drainage basins) due to dry climate conditions. We should note that several ocean sediment cores to the northwest of the Amazon River show a relatively increased sediment rate during HS1 (Fig. 4a), possibly caused by the weakness or reversal of the North Brazil Current and the increase in sea level related to ice sheet melting (Zhang et al. 2015). These could mute the continental runoff signals and complicate the interpretation of the sediment rate change. To summarize, a combination of multisource paleoclimate proxies, including speleothem $\delta^{18}O_c$, land and ocean sediments, tends to suggest a millennial dipole response in precipitation and $\delta^{18}O$ over the lowland TSA region, justifying the model performance on millennial hydroclimate response over the TSA.

Time series from reconstructed speleothems and ocean sediment cores and from our model (Figs. 3 and 4) suggest that the millennial variability of hydroclimate over the TSA is closely related to the change of AMOC intensity [Fig. 3d(1)] and is driven by the meltwater discharging into the North Atlantic Ocean [Fig. 3c(1)]. In addition, the coherent $\delta^{18}O_c$ temporal variability pattern in eastern Brazil is out of phase with that in the East Asian monsoon region in our model and the observation, consistent with previous proxy studies (Cheng et al. 2012). However, the out-of-phase correlation on $\delta^{18}O_c$ is not accompanied by a similarly out-of-phase correlation between SASM and East Asian monsoon intensity, a point to be returned later. One should note that the only Amazonia speleothem cave Paraíso is located at the intermediate zone of the modeled dipole (in terms of ANN precipitation shown in Fig. 4a). Thus, a small displacement of the model dipole will cause the discrepancy of $\delta^{18}O_c$ between the model and the speleothem [Fig. 3a(2)].

5. The hydroclimate footprint and mechanism

a. *Large-scale spatial–temporal pattern*

As we just mentioned, our model reasonably simulates a comprehensive spatial–temporal pattern of the millennial hydroclimate variability, which can be utilized to study physical mechanisms. Here, we conducted a combined empirical orthogonal function (CEOF) analysis on precipitation and $\delta^{18}O_p$ (temporarily excluding the effect of cave temperature) during the last deglaciation to extract the leading modes of $\delta^{18}O_p$–monsoon precipitation over the TSA. The first two modes, CEOF1 (Fig. 5) and CEOF2 (Fig. 6), explain 42% and 26% of the total variance, respectively. We only focus on DJF in the following discussions because the basic northwest–southeast dipole structure that emerges in the ANN is driven by the DJF anomalies (Figs. S1–S3).

The first CEOF mode (PC1; Fig. 5) shows a distinguished millennial variability with the spatial patterns dominated by a general northwest–southeast (NW–SE) dipole in precipitation and $\delta^{18}O_p$ of the opposite signs (in the sense of amount effect). The SE pole is in the eastern Brazil region, while the NW pole is in the western Amazon region (Figs. 5a,b). The millennial variability of NW–SE dipoles links to the meridional migration of ITCZ (Fig. 5c), which is, in turn, correlated with the AMOC intensity and the meltwater discharge in the North Atlantic basin (Fig. 5c). The corresponding surface temperature is characterized by an opposite response in the two hemispheres (Fig. 5d), associated with the so-called bipolar seesaw response (Kanner et al. 2012; Stríkis et al. 2015; Wang et al. 2017). The dominant role of meltwater forcing is further supported by the meltwater forcing effect derived from the sensitivity experiments (iTRACE minus ICE+ORB+GHG), as seen in the deglacial evolution from sites in both dipole regions (Fig. 7). Quantitatively, the average variance contributions of meltwater forcing to the variability of DJF precipitation, $\delta^{18}O_p$, and surface temperature are 77%, 93%, and 24%, respectively (Fig. S6; see methods for detail). The pattern of rainfall and $\delta^{18}O_p$ associated with the PC1 can also be seen in the difference between HS1 (15.8–15.2 ka) and LGM (20–19 ka) as a response to increased meltwater flux and, in turn, decreased AMOC, or similarly, in the difference between BA (13.6–13 ka) as a response to decreased meltwater flux or increased AMOC (Figs. S2b and S3b; Fig. 4a; Figs. 5a,b). The simulated dipole pattern response in millennial precipitation and $\delta^{18}O_p$ is also supported by the compiled speleothems (Fig. 3), land and ocean sediment records (Fig. 4), as well as with idealized snapshot and hosing simulations in different climate models (Jackson et al. 2015; Campos et al. 2019).

The second CEOF mode (PC2; Fig. 6) shows a homogenous surface warming trend during the last deglaciation and a similar NW–SE dipole in precipitation and $\delta^{18}O_p$ to the first mode, albeit with a bit of location difference. The long-term trend in PC2 is consistent with the decreased austral summer insolation, increased CO_2 concentration, and reduced continental ice sheet volume, indicating likely the insolation, GHG, and ice sheet as the driving factors for the SASM rainfall at the orbital time scale. The primary contribution of GHG forcing on surface temperature is supported by the GHG impact isolated from the sensitivity experiments (GHG+ORB+ICE minus ORB+ICE), as seen in the deglacial evolution over the TSA region [Figs. 7c(1)–c(5) and 8i]. The contribution of GHG, insolation, and ice sheet forcing to TSA precipitation are roughly comparable, with an average variance contribution of 14%, 12%, and 10%, respectively (Fig. S6; see methods for detail). The dipole response in precipitation and $\delta^{18}O_p$, can be seen in the insolation-alone sensitivity experiments (ORB in

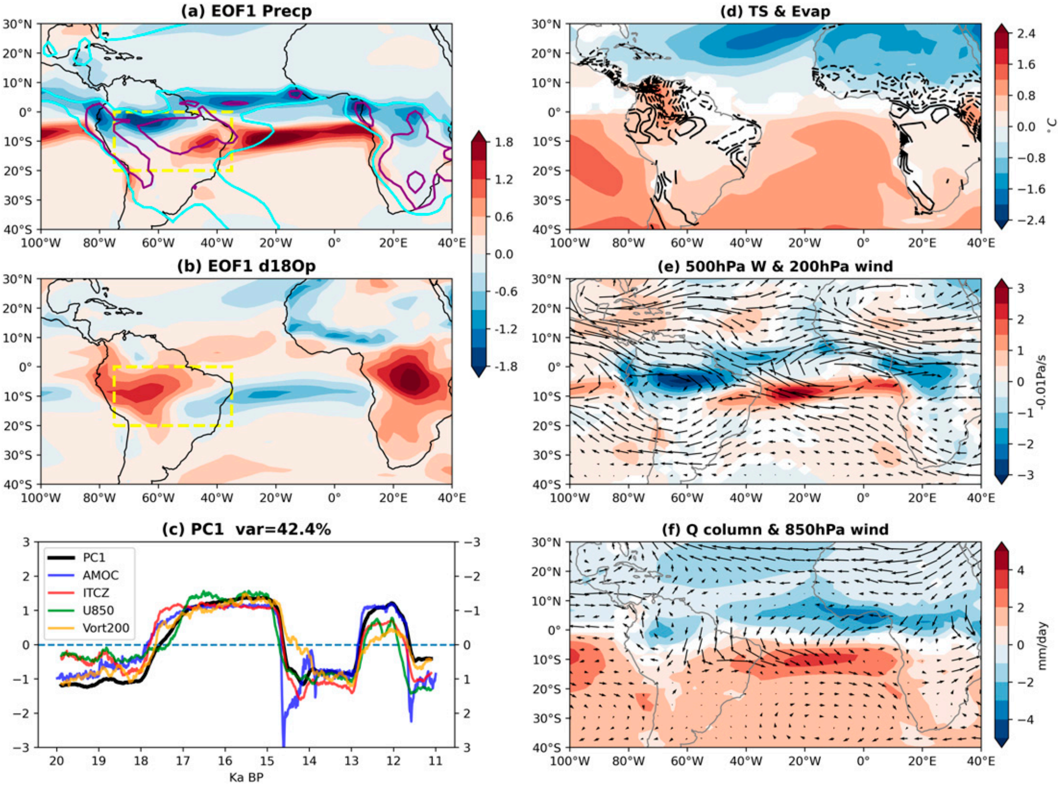

FIG. 5. CEOF1 on DJF precipitation and $\delta^{18}O_p$ and associated SASM hydroclimate footprint based on iTRACE experiment. Spatial pattern of (a) precipitation and (b) $\delta^{18}O_p$ for CEOF1. Cyan and purple lines in (a) are DJF precipitation with the intensity of 3 and 6 mm day^{-1} for LGM climatology. The yellow dashed frame denotes the dipole region. (c) Time series of normalized time coefficients of the first CEOF mode (PC1: black; left axis), model AMOC intensity (blue line; right axis), and latitudinal ITCZ position (red line; right axis. The latitudinal ITCZ position is calculated as the latitude of maximum precipitation $\phi_{\max}$ within tropics, following Adam et al. (2016): $\phi_{\max} = \int_{20°S}^{20°N} \phi(\cos\phi P)^{10} d\phi / \int_{20°S}^{20°N} (\cos\phi P)^{10} d\phi$, where P is precipitation and ϕ is latitude); easterly intensity: the absolute magnitude of zonal wind at 850 hPa over the TSA (10°S–0°, 60°–40°W; green line for right axis), and vorticity intensity at 200 hPa in Bolivia (24°–14°S, 75°–65°W; yellow line for right axis). Note that all the time series are standardized and moving averaged by 200 years for visualization. Regression maps of hydroclimate footprint on PC1: (d) surface temperature (shading) and evapotranspiration (contours; in mm day^{-1}); (e) vertical velocity at 500-hPa level (shading) and wind at 200 hPa level (vectors; in 5 m s^{-1}); (f) precipitable water (shading; in mm day^{-1}) and 850 hPa wind (vectors; in 5 m s^{-1}). Regression fields over 99% ($P < 0.01$) confidence level using the two-tailed Student's t test are plotted.

Figs. 8a,b), while ice sheet (ORB+ICE in Figs. 8d,e) further enhances the amplitude of the dipole response driven by insolation. Specifically, during the last deglaciation (from LGM to YD), reduced DJF insolation and ice sheet volume produce similar dipole responses: precipitation increases in northeastern Brazil and decreases from western Amazon to southern coastal Brazil. Increased GHG, however, produces a dipole with increased precipitation in central-west Amazon and decreased precipitation in northeastern Brazil (not shown), which, to some extent, counterbalance the dipole induced by insolation and ice sheet change (ORB+ICE+GHG in Figs. 8g,h). The insolation-driven dipole response in rainfall/$\delta^{18}O_p$ on the orbital time scale is consistent with speleothem records and snapshot simulations that are shown in previous studies (Cruz et al. 2009; Cheng et al. 2013; Liu and Battisti 2015). The GHG-driven dipole response in rainfall/$\delta^{18}O_p$ is consistent with previous high CO_2 concentration paleoclimate simulations (Liu et al. 2020) and is also supported by the speleothem record from cave Paraíso, which suggests that CO_2 can influence regional convection in the eastern Amazon lowlands (Wang et al. 2017).

Until now, we have only considered the spatial–temporal millennial response of $\delta^{18}O_p$ and precipitation. To investigate the effect of local surface or cave temperature on the results above, we repeat the CEOF decomposition analysis but on $\delta^{18}O_c$ and precipitation. The results show a very similar CEOF1 mode to the former one for both precipitation and $\delta^{18}O_c$ (comparing Figs. S4a,b to Figs. 5a,b), explaining 40% of the total variance. This coincides with our expectation as the effect of temperature on $\delta^{18}O_c$ value is negligible in the millennial time scale (see section 2c). The CEOF2 mode increases its variance explanation from 26% to 32%. The spatial pattern on CEOF2 is similar to the former one for

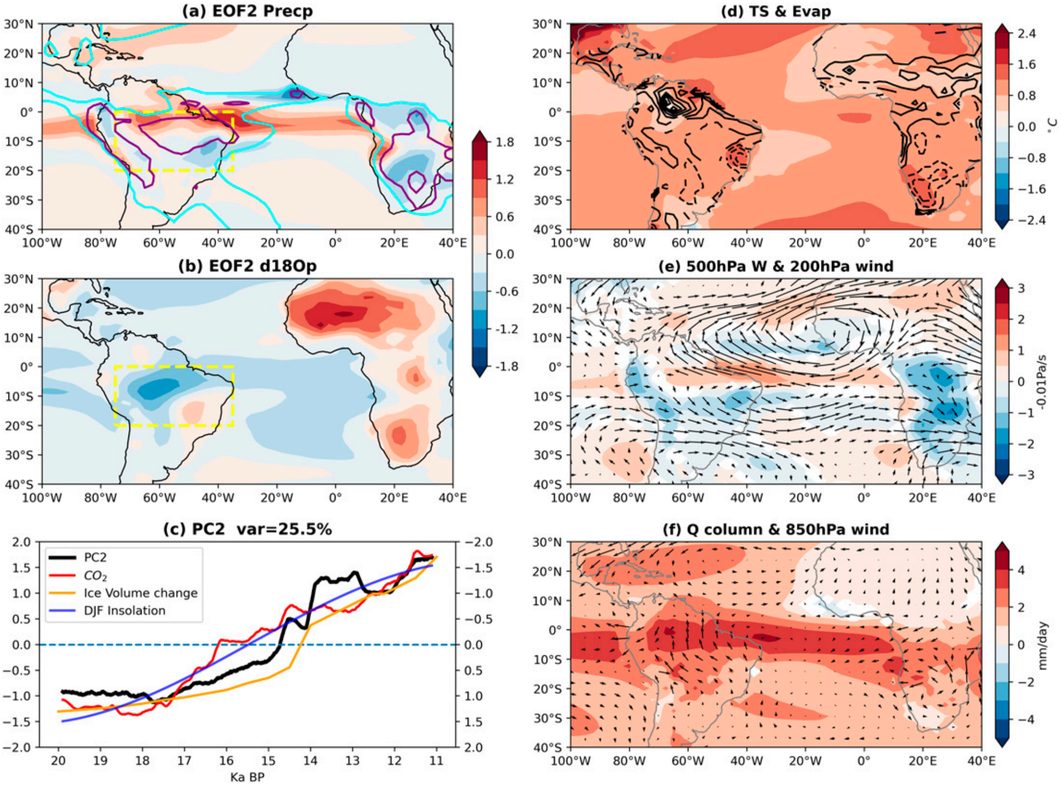

FIG. 6. CEOF2 on DJF precipitation and $\delta^{18}O_p$ and associated SASM hydroclimate footprint based on iTRACE experiment. (a),(b) As in Fig. 5, but for CEOF2. (c) Time series of normalized time coefficients of the second CEOF mode (PC2: black line for left axis), global mean CO_2 concentration (red line for left axis), global ice volume change since LGM (orange line for right axis) and DJF insolation at 15°S (blue line for right axis). Note that all the time series are standardized and moving averaged by 200 years. (d)–(f) As in Fig. 5, but for regression maps of the hydroclimate footprint on PC2. Regression fields over 99% ($P < 0.01$) confidence level using the two-tailed Student's t test are plotted.

precipitation, but for $\delta^{18}O_c$, the magnitude of the dipole response somewhat deviates (comparing Figs. S4c,d to Figs. 6a,b). The central-northern Amazon shows a larger amplitude of $\delta^{18}O_c$ change, while eastern Brazil has a smaller amplitude of $\delta^{18}O_c$ change. The more depleted $\delta^{18}O_c$ over the South American continent caused by general surface or cave warming during the last deglaciation modulates the dipole pattern in $\delta^{18}O_c$ (Fig. 6) to be less significant compared to $\delta^{18}O_p$.

Overall, in spite of the different forcing mechanisms and temperature responses between the two CEOF modes, the NW–SE dipole pattern responses in rainfall/$\delta^{18}O_p$ are roughly similar between the two (Figs. 5a,b vs Figs. 6a,b). Thus, the dipole pattern of SASM precipitation and $\delta^{18}O_p$ ($\delta^{18}O_c$) is a robust response feature for both millennial (CEOF1 mode) and orbital scales (CEOF2 mode). This highlights the inherent stability of the spatial characteristics of the SASM regardless of the external forcing and time scales, as similar cases are also suggested in centennial-scale variability (Orrison et al. 2022). During the deglaciation, global external forcings (GHG, austral summer insolation, and ice sheet forcing) can either counter the effect of meltwater forcing at LGM and YD, or reinforce the effect of meltwater forcing at HS1 and BA, strengthening or weakening the meltwater forced NW–SE dipole.

b. *Mechanism of precipitation response*

The evident dipole response in millennial variability of SASM precipitation and $\delta^{18}O_p$ can be attributed to atmospheric circulation anomalies resulting from meltwater forcing. The effects of increased meltwater forcing can also be observed in the difference between HS1 and LGM, which indicates a weakened AMOC and a southward displacement of ITCZ, along with a southward migration of the Hadley cell and an increased low-level northern wind (Fig. 5f). As the system migrates southward, a reduction in low-level southeasterly winds and anomalous moisture convergence weaken the subsidence, coupled with decreased upper-tropospheric Nordeste low, and eventually increased precipitation in eastern Brazil or the SE pole (Figs. 5c,e,f). Meanwhile, the weakened low-level easterly wind and anomalous moisture divergence, along with the weakened upper-tropospheric Bolivia high, suppresses the ascending motion and reduces the rainfall in the central-western TSA region or the NW pole (Figs. 5c,e,f). This, in general, suggests a weaker regional Walker circulation within the hemisphere. In

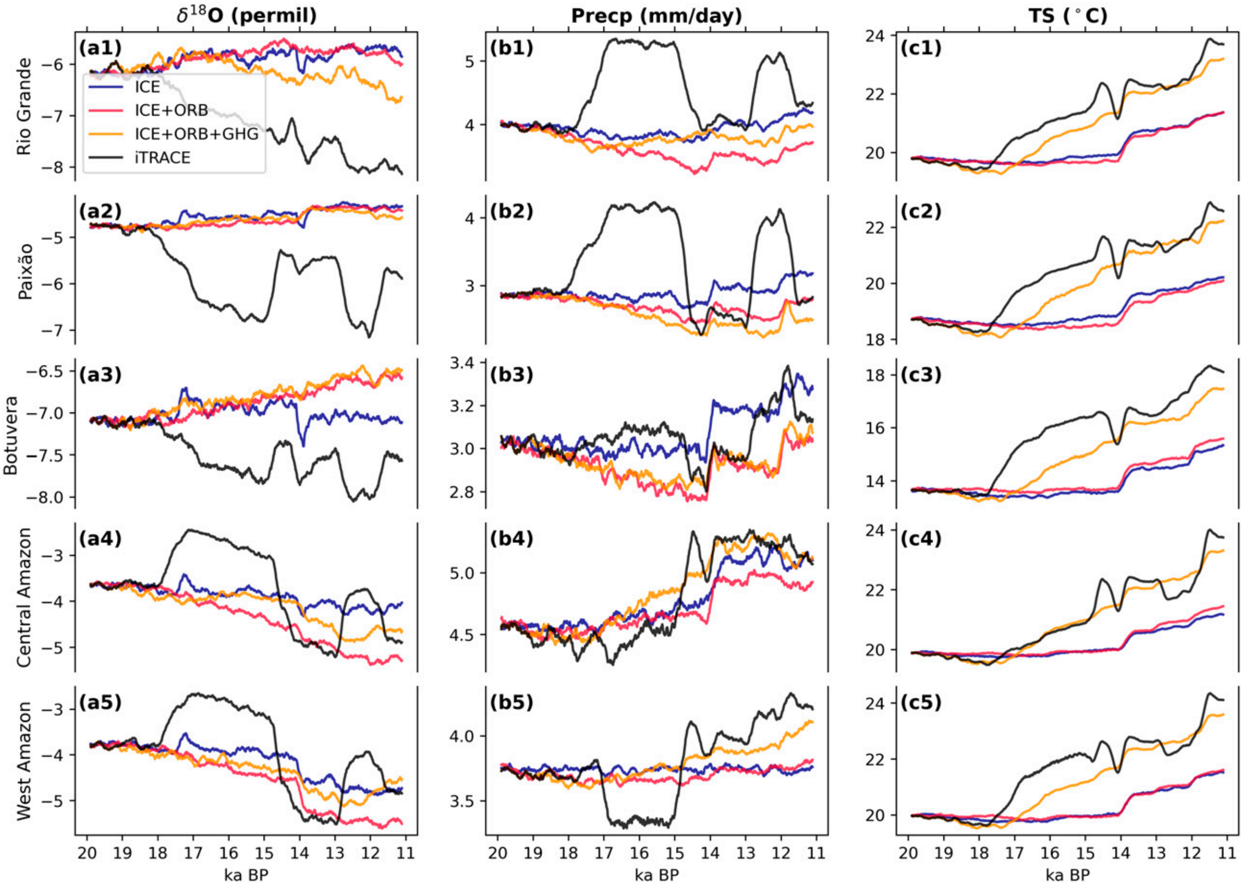

FIG. 7. Hydroclimate and $\delta^{18}O_c$ evolution over the TSA region in four deglacial sensitivity experiments. [a(1)]–[a(5)] Annual $\delta^{18}O_c$ (‰); [b(1)]–[b(5)] precipitation (mm day^{-1}); [c(1)]–[c(5)] surface temperature (°C). Model results have been smoothed with a 200-yr running mean for ICE (blue), ICE+ORB (red), ICE+ORB+GHG (orange), ICE+ORB+GHG+MWF, and iTRACE (black). (top three rows) Rio Grande, Paixão, and Botuvera in eastern Brazil (SE pole); (bottom two rows) central (3°S, 55°W) and western Amazon (7°S, 65°W) (NW pole).

addition, we note that the change of the SACZ intensity (usually defined as precipitation in the NW–SE convection zone in southeastern Brazil) is not obvious, causing a relatively small hydroclimate response in the subtropical South American continent.

The dynamical origin of dipole response over the TSA is from the balance between the changes in Bolivian high and in Nordeste low, which is possibly triggered by an upper-tropospheric Rossby wave induced by diabatic heating from the western Amazon convection region (Cruz et al. 2009; Orrison et al. 2022). The dipole rainfall response in TSA is, therefore, robust because the rainfall response in the central-western Amazon (NW pole) is dynamically linked to that in eastern Brazil (SE pole) through both lower- and upper-level atmospheric circulation of the SASM system.

The atmospheric circulation anomalies resulting in the dipole are also likely consistent with the response to global external forcings on the orbital time scale. Decreased austral summer (DJF) insolation during the deglaciation causes a continental cooling effect and thus a decreased SACZ and weakened SASM (Figs. 8a–c). Besides, ITCZ tends to be displaced slightly northward and strengthens, producing a north–south dipole of vertical velocity (not shown) and thus a north–south dipole of precipitation and $\delta^{18}O_p$ over the TSA (Figs. 8a,b), consistent with Liu and Battisti (2015) and Cruz et al. (2009). Decreased ice sheet volume reverses the cooling effect from decreased DJF insolation and tends to produce a local response in TSA precipitation and amplify the response of insolation (Figs. 8d,e), and detailed mechanisms remain to be explored in the future. Increased GHG forcing during the last deglaciation (Figs. 6c and 8i) produces a homogeneous surface warming and increased precipitable water over the tropical and subtropical continent, following the Clausius–Clapeyron relationship (Figs. 6d,f) (Allen and Ingram 2002). Increased GHG also warms the surface of the tropical Atlantic Ocean, which increases seawater evaporation and hence moisture transport into South American continent (Liu et al. 2020).

As the surface or cave temperature effect is important in affecting $\delta^{18}O_c$ at the orbital time scale, we repeat analysis on $\delta^{18}O_c$ for sensitivity simulations on each forcing factor, and the results are shown in Fig. S5 (comparing that with $\delta^{18}O_p$ in Fig. 8). Similar to the spatial pattern in CEOF2, the dipole

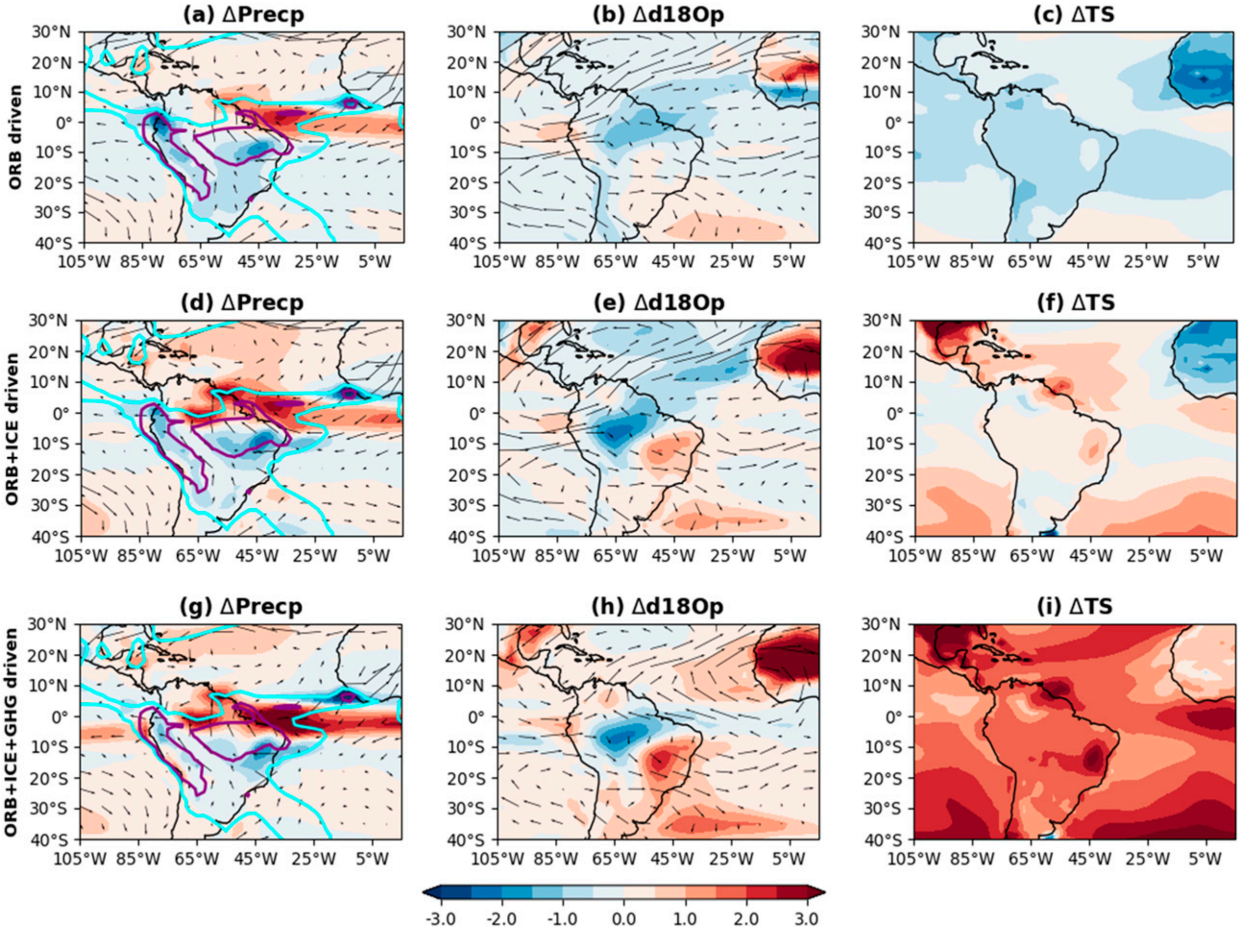

FIG. 8. Response of precipitation (mm day^{-1}), $\delta^{18}O_p$ (‰), and surface temperature (°C) to (a)–(c) orbital forcing; (d)–(f) orbital and ice sheet forcing; and (g)–(i) orbital, ice sheet, and GHG forcing. Response is calculated as the difference between YD (12.6–12 ka) and LGM (20–19 ka) from four sensitivity experiments. Overlayed vectors in (a), (d), and (g) are wind vectors at the 850-hPa level. Overlayed vectors in (b), (e), and (h) are wind vectors at the 200-hPa level. Cyan and purple contours in (a), (d), and (g) are DJF precipitation with the intensities of 3 and 6 mm day^{-1} for LGM climatology.

response of $\delta^{18}O_c$ to general warming during the last deglaciation (YD minus LGM) tends to increase (decrease) its amplitude in central-northern Amazon (eastern Brazil), showing a less clear dipole. This is mainly explained by increased GHG-induced warming (Fig. S5).

c. *The responses of the millennial SASM intensity*

Given the dipole response of the TSA precipitation and $\delta^{18}O_p$ at the millennial time scale, one should be cautious utilizing $\delta^{18}O_p$ from eastern Brazil or Andes (where most speleothem records are available) as an indicator to infer the millennial SASM intensity change. Some previous studies (Kanner et al. 2012; Stríkis et al. 2015, 2018) interpreted the depletion of $\delta^{18}O_p$ over eastern Brazil and Andes as evidence of increased rainfall and SASM intensity. However, the east Brazil region corresponds only to the SE pole of the dipole response, while the NW pole response tends to be the opposite. Thus, the SE pole may not be reliable for inferring the past SASM intensity. The Andes, characterized by a narrow elevated topography, experiences different local atmospheric circulation, moisture source, and possibly different factors controlling $\delta^{18}O$ values compared to the vast lowland region (Vuille et al. 2003b). Whether alpine Andes records [cave Pacupahuain (Kanner et al. 2012) and ice core Huascarán (Thompson et al. 1995)] document the moisture change associated with SASM intensity is still a controversial topic (Thompson et al. 1995; Vuille et al. 2003b; Samuels-Crow et al. 2014). We also note the availability of low-altitude tropical Andes records such as cave Santiago (Mosblech et al. 2012) and Cueva del Diamante (Cheng et al. 2013). However, we are unable to justify their connection to SASM intensity due to the coarse model resolution and model–proxy discrepancy. Here, we will propose a robust indicator for SASM intensity based on lowland Amazon hydroclimate response.

Indeed, increased precipitation (depleted $\delta^{18}O_p$) in the SE pole is related to the southward migration of Atlantic ITCZ, which is also linked dynamically to a reduction of the low-level easterly monsoon wind and weakened upper troposphere Bolivia high and, in turn, a reduction of rainfall inland

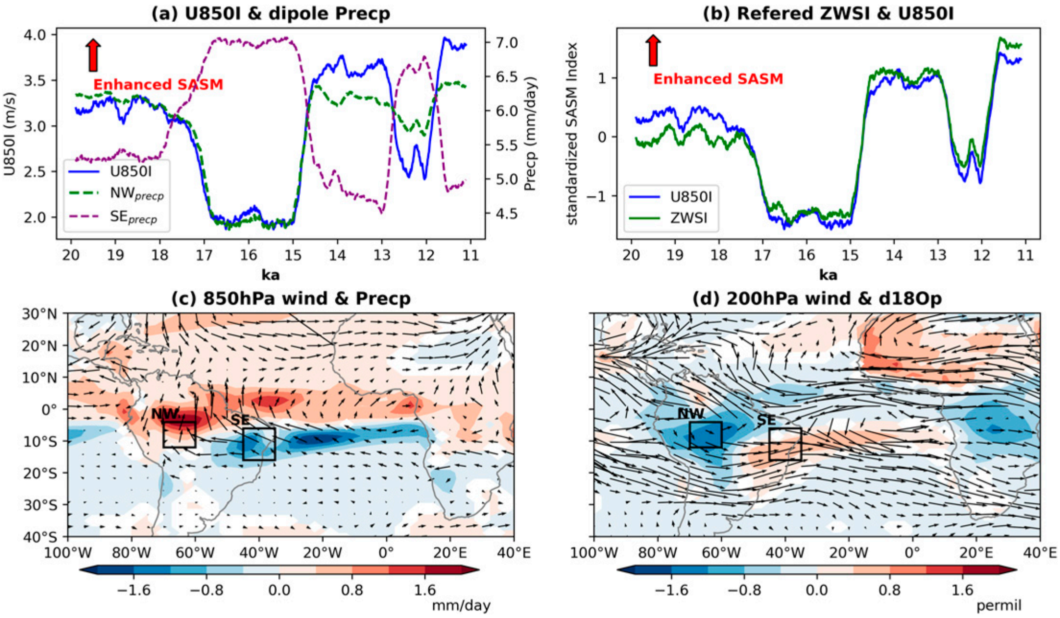
(a) U850I & dipole Precp

(b) Refered ZWSI & U850I

(c) 850hPa wind & Precp

(d) 200hPa wind & d18Op

FIG. 9. (a) Time series of low-level zonal wind index at 850-hPa level (U850I) over the TSA (15°–10°S, 60°–40°W; solid blue line for left axis; units: m s^{-1}). Also shown is the time series of regional precipitation in the NW pole (dashed green line for right axis) and the SE pole (dashed purple line for right axis) (in mm day^{-1}). (b) Time series of standardized U850I (blue line) is highly correlated with standardized ZWSI (green line) referred from Gan et al. (2005). (c),(d) Regression maps of hydroclimate footprint on U850I: (c) precipitation and 850-hPa wind; (d) $\delta^{18}O_p$ and 200 hPa wind. The hydroclimate response in (c) and (d) is similar to that in Fig. 5, but with the opposite sign, indicating that the low-level zonal wind represents the millennial SASM intensity change. Regression fields over 99% ($P < 0.01$) confidence level using the two-tailed Student's t test are plotted.

in the NW pole (Figs. 5e,f). Due to the robust dynamic link of the monsoon wind for regional rainfall, we propose that the low-level southeasterly wind is a better indicator of millennial SASM change over the tropical region (TSA). As such, we define the low-level zonal wind index (U850I) as the 850 hPa zonal wind intensity averaged within 15°–5°S, 60°–40°W as an indicator of SASM intensity. The regression map of the atmospheric footprint on U850I (Figs. 9c,d) shows that a stronger southeasterly monsoon wind increases moisture convergence and, in turn, rainfall (with depleted $\delta^{18}O_p$) downstream in the inland Amazon region (NW pole), but decreases moisture convergence and, in turn, rainfall (with enriched $\delta^{18}O_p$) upstream in the eastern Brail region (SE pole), representing an intensified regional Walker circulation and SASM intensity from its climatological mean (Fig. 1d vs Fig. 9c). Therefore, SASM intensity tends to increase (decrease) in response to decreased (increased) meltwater discharge. Note that our zonal wind index U850I for SASM millennial variability is consistent with the indices of interseasonal and interannual variability of SASM. As an example, we show that our index U850I is highly correlated with the zonal wind shear index (ZWSI; the difference of zonal wind between 200 and 850 hPa in central Brazil) defined by Gan et al. (2005) (Fig. 9b), which means ZWSI can also be used similarly for deglaciation. Overall, considering the dipole response, depleted $\delta^{18}O_p$ or increased precipitation in eastern Brazil (for the millennial time scale) tends to indicate a decreased SASM intensity over the TSA.

6. Conclusions and discussion

To understand hydroclimate variability and forcing mechanisms of the TSA during the last deglaciation (20–11 Ka before the present), we conducted a series of transient climate simulations of climate variables and water isotopes (iTRACE) with the state-of-art isotope-enabled Community Earth System Model (iCESM). Specifically, this study shows the following:

1) Our model, in general, qualitatively reproduces the $\delta^{18}O_c$ evolution during the last deglaciation over the eastern TSA region. However, the magnitude of $\delta^{18}O_c$ variability tends to be underestimated compared with the proxies, which suggests that the model may fail to capture some dynamic or physical processes and thus be unable to explain specific paleoclimate events thoroughly. The variability in $\delta^{18}O_c$ or $\delta^{18}O_p$ varies with local precipitation change in the sense of amount effect and, therefore, may be used qualitatively as an indicator of local rainfall.
2) The SASM exhibits a robust NW–SE dipole response over TSA in precipitation and $\delta^{18}O_p$ at both millennial and orbital scales. This highlights the inherent stability of the spatial characteristics of the SASM regardless of the external forcing and time scales. The millennial-scale dipole of precipitation and $\delta^{18}O_p$ are driven by meltwater forcing and AMOC intensity, corresponding to ITCZ meridional migration and associated Walker circulation change. The millennial SASM over the TSA, indicated by

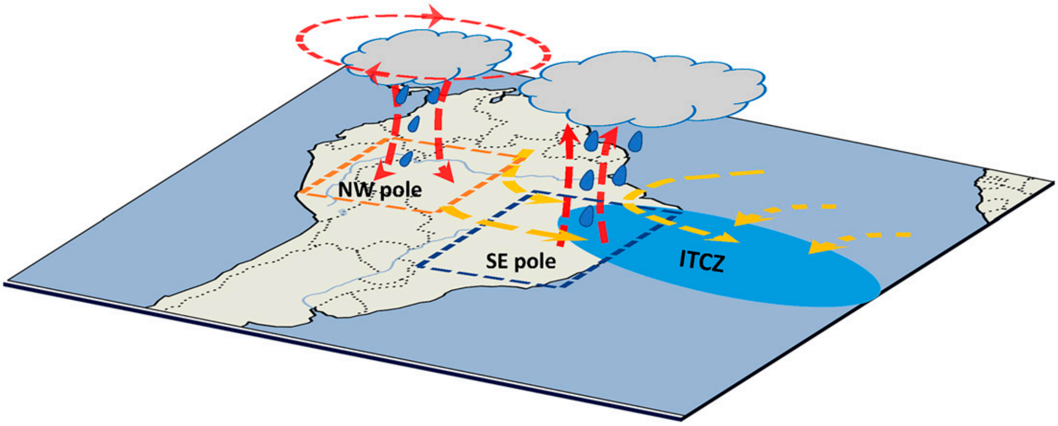

FIG. 10. Schematic figure for the mechanism of the TSA precipitation response to meltwater forcing (HS1 − LGM). For the mechanism of millennial precipitation response, a southward displacement of the ITCZ and ascending branch of the Hadley cell produces the low-level convergence, anomalous low-level northwesterly wind, and thus anomalous wet conditions in eastern Brazil (SE pole). In contrast, decreased low-level easterly and anomalous subsidence correspond to a decreased Bolivia high, producing an abnormal dry condition in the central-western Amazon (NW pole) and, thus, reduced SASM intensity over the TSA. Note that all dashed vectors denote the atmospheric circulation anomalies.

the low-level zonal wind and precipitation/$\delta^{18}O_p$ in the midwestern Amazon, tends to be weakened in response to meltwater discharge, as summarized schematically in Fig. 10. The orbital-scale dipole of precipitation and $\delta^{18}O_p$ are driven by austral summer insolation, which is further reinforced ice sheet forcing but counterbalanced by GHG forcing. The highlighted millennial dipole response in the lowland TSA region is supported by multisource paleoclimate proxies, including speleothems and land and ocean sediments, as well as climate model simulations from other institutes.

One should note that the aforementioned mechanisms on dipole response in millennial and orbital time scales may not be the "perfect" results. The discrepancy between the model and speleothem $\delta^{18}O_c$, mostly the underestimated millennial $\delta^{18}O_c$ ($\delta^{18}O_p$) variability, suggested likely further drivers that the model is not capturing and, therefore, insufficient to explain specific paleoclimate events. One potential model deficiency from model tropical sea surface temperature (SST) bias (not shown) may affect model performance in simulating TSA precipitation. After removing the effect of tropical SST bias on simulated precipitation and $\delta^{18}O_p$ (see methods), the millennial dipole response (HS1–LGM) is still robust compared to the original iTRACE simulations, albeit the extent and amplitude of the dipole regions may vary (Fig. 11). Specifically, the SE dipole in northeastern Brazil and the NW dipole in the Amazon region expand less southward to the subtropics. The amplitude of the NW pole response reduces in ANN, but not too much difference in DJF. Therefore, the proposed mechanisms of millennial SASM hydroclimate (for DJF) still hold. One encouraging improvement is that the model $\delta^{18}O_p$ millennial variability (HS1–LGM) significantly increased and is closer to the variability of proxy $\delta^{18}O_c$ in cave Rio Grande, Jaraguá, and Botuvera, whose variability is underestimated in original iTRACE simulations (comparing labeled $\delta^{18}O_p/\delta^{18}O_c$ values in Fig. 11). We also repeat the annual cycle analysis as in Fig. 2 based on corrected SST simulations. However, the precipitation "double ITCZ" bias remains in Manaus (Amazon region). The precipitation-weighted ANN $\delta^{18}O_p$ will deviate from the actual value if the seasonal cycle of precipitation is incorrect, which may cause the discrepancy of $\delta^{18}O_p$ ($\delta^{18}O_c$) between the model and the only central Amazon proxy in Paraíso (Fig. 3a2). However, the ANN discrepancy in cave Paraíso alone cannot refute the existence of the NW pole in DJF for two reasons: 1) the cave is located at the intermediate zone of the modeled dipole in terms of ANN precipitation (Fig. 4a), which means a small displacement of the model dipole will cause the discrepancy of $\delta^{18}O_c$ between the model and speleothem. 2) The response of the NW pole in DJF is offset by JJA (austral winter), which tends to mute the response in ANN (Figs. S2 and S3; Fig. 4b). Our study, therefore, poses the necessity to build more direct paleoclimate proxy data in the central-west Amazon region to comprehensively understand millennial hydroclimate change over the TSA.

Another source of the model–proxy discrepancy may be from the model resolution: coarse model grids may not capture the subgrid physics and tend to underestimate rainfall and $\delta^{18}O_p$ in the Amazon region (Goswami and Goswami 2017). We also note the model $\delta^{18}O_c$ is empirically derived from Eqs. (1)–(3) rather than calculated from the forward model, which explicitly considers the carbonate chemistry evolution as precipitated water moves down to the soil, the epikarst, and eventually into the cave (Tabor et al. 2021). The drip water transmitted to the karst system is modulated by evaporation and storage in the soil, recharge rates, subsurface mixing, and varying water residence times (Comas-Bru et al. 2019). Besides, whether speleothem temperature was tracking

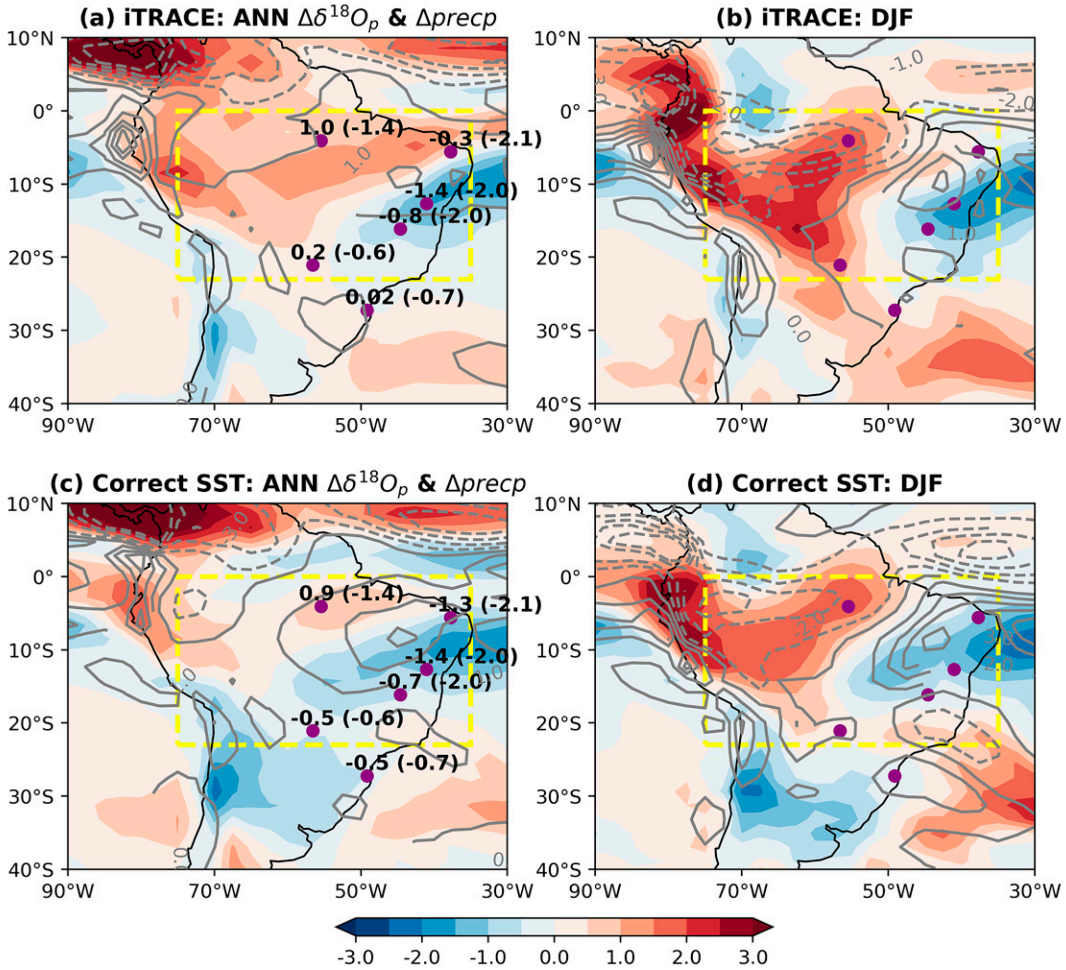

FIG. 11. Response of $\delta^{18}O_p$ (shading; in ‰) and precipitation (contours; in mm day^{-1}) to meltwater: the difference between HS1 (15.8–15.2 ka) and LGM (20–19 ka) from (a),(b) original iTRACE experiment and (c),(d) SST bias corrected experiment. (a),(c) Annual mean; (b),(d) DJF. Labeled values outside and inside the parentheses are for change of $\delta^{18}O_p$ (HS1 − LGM) in the model simulation and change of $\delta^{18}O_c$ in speleothem proxies, respectively. The yellow dashed frame denotes the dipole region over the TSA.

surface temperature is uncertain. All the aforementioned factors may cause uncertainty of the modeled $\delta^{18}O_c$ in this study and could be part of the origin of discrepancy in model–proxy $\delta^{18}O_c$ comparison (section 4). Explaining and reconciling the discrepancy between the climate model and paleoclimate proxies is a challenging task in the tropical monsoon region and deserves further studies in the future.

Finally, it is interesting to point out that, although the dipole response of precipitation in SASM resembles that in the EASM region, the dipole $\delta^{18}O_p$ response in the SASM region is in contrast to the homogeneous $\delta^{18}O_p$ response over the EASM region (Liu et al. 2014; He et al. 2021a). This suggests a different relation between $\delta^{18}O_p$ and rainfall between the two monsoon regions. Mechanisms of the dipole $\delta^{18}O_p$ response to the SASM will be studied in detail in Bao et al. (2023).

Acknowledgments. We thank Drs. L. Thompson and E. Mosley-Thompson for helpful discussions. Our deepest gratitude goes to the reviewers for their dedicated work and insightful comments/suggestions that have helped improve this paper. This work is supported by LSKJ202203300 and U.S. NSF AGS2002506, AGS2002521. The CESM project is supported primarily by the National Science Foundation (NSF). This material is based on work supported by the National Center for Atmospheric Research, which is a major facility sponsored by the NSF under Cooperative Agreement 1852977. Computing and data storage resources, including the Cheyenne supercomputer (https://doi.org/10.5065/D6RX99HX), were provided by the Computational and Information Systems Laboratory (CISL) at NCAR.

Data availability statement. All iTRACE simulation data used in this study can be found at https://www.earthsystemgrid.org/dataset/ucar.cgd.ccsm4.iTRACE.html. Paleoclimate proxy data could be found from NOAA (https://www.ncdc.noaa.gov/data-access/paleoclimatology-data). The present-day water isotope observation data (GNIP) can be found from the

International Atomic Energy Agency (https://www.iaea.org/services/networks/gnip).

REFERENCES

Adam, O., T. Bischoff, and T. Schneider, 2016: Seasonal and interannual variations of the energy flux equator and ITCZ. Part I: Zonally averaged ITCZ position. *J. Climate*, **29**, 3219–3230, https://doi.org/10.1175/JCLI-D-15-0512.1.

Allen, M. R., and W. J. Ingram, 2002: Constraints on future changes in climate and the hydrologic cycle. *Nature*, **419**, 228–232, https://doi.org/10.1038/nature01092a.

Argus, D. F., W. R. Peltier, R. Drummond, and A. W. Moore, 2014: The Antarctica component of postglacial rebound model ICE-6G_C (VM5a) based on GPS positioning, exposure age dating of ice thicknesses, and relative sea level histories. *Geophys. J. Int.*, **198**, 537–563, https://doi.org/10.1093/gji/ggu140.

Battisti, D. S., Q. Ding, and G. H. Roe, 2014: Coherent pan-Asian climatic and isotopic response to orbital forcing of tropical insolation. *J. Geophys. Res. Atmos.*, **119**, 11–997, https://doi.org/10.1002/2014JD021960.

Bao, Y., Z. Liu, and C. He, 2023: Dipole response of millennial variability in tropical South American precipitation and $\delta^{18}O_p$ during the last deglaciation. Part II: $\delta^{18}Op$ response. *J. Climate*, **36**, 4709–4721, https://doi.org/10.1175/JCLI-D-22-0289.1.

Brady, E., and Coauthors, 2019: The connected isotopic water cycle in the Community Earth System Model version 1. *J. Adv. Model. Earth Syst.*, **11**, 2547–2566, https://doi.org/10.1029/2019MS001663.

Buizert, C., and Coauthors, 2021: Antarctic surface temperature and elevation during the Last Glacial Maximum. *Science*, **372**, 1097–1101, https://doi.org/10.1126/science.abd2897.

Burckel, P., C. Waelbroeck, J. M. Gherardi, S. Pichat, H. Arz, J. Lippold, T. Dokken, and F. Thil, 2015: Atlantic Ocean circulation changes preceded millennial tropical South America rainfall events during the last glacial. *Geophys. Res. Lett.*, **42**, 411–418, https://doi.org/10.1002/2014GL062512.

Campos, M. C., and Coauthors, 2019: A new mechanism for millennial scale positive precipitation anomalies over tropical South America. *Quat. Sci. Rev.*, **225**, 105990, https://doi.org/10.1016/j.quascirev.2019.105990.

Cheng, H., A. Sinha, X. Wang, F. W. Cruz, and R. L. Edwards, 2012: The Global Paleomonsoon as seen through speleothem records from Asia and the Americas. *Climate Dyn.*, **39**, 1045–1062, https://doi.org/10.1007/s00382-012-1363-7.

——, and Coauthors, 2013: Climate change patterns in Amazonia and biodiversity. *Nat. Commun.*, **4**, 1411, https://doi.org/10.1038/ncomms2415.

Comas-Bru, L., S. P. Harrison, M. Werner, K. Rehfeld, N. Scroxton, and C. Veiga-Pires, 2019: Evaluating model outputs using integrated global speleothem records of climate change since the last glacial. *Climate Past*, **15**, 1557–1579, https://doi.org/10.5194/cp-15-1557-2019.

Cook, K. H., 2009: South American climate variability and change: Remote and regional forcing processes. *Past Climate Variability in South America and Surrounding Regions*, Springer, 193–212.

Coplen, T. B., C. Kendall, and J. Hopple, 1983: Comparison of stable isotope reference samples. *Nature*, **302**, 236–238, https://doi.org/10.1038/302236a0.

Cruz, F. W., and Coauthors, 2005: Insolation-driven changes in atmospheric circulation over the past 116,000 years in subtropical Brazil. *Nature*, **434**, 63–66, https://doi.org/10.1038/nature03365.

——, and Coauthors, 2009: Orbitally driven east–west antiphasing of South American precipitation. *Nat. Geosci.*, **2**, 210–214, https://doi.org/10.1038/ngeo444.

Dansgaard, W., 1964: Stable isotopes in precipitation. *Tellus*, **16**, 438–468, https://doi.org/10.1111/j.2153-3490.1964.tb00181.x.

Deininger, M., B. M. Ward, V. F. Novello, and F. W. Cruz, 2019: Late quaternary variations in the South American monsoon system as inferred by speleothems—New perspectives using the SISAL database. *Quaternary*, **2**, 6, https://doi.org/10.3390/quat2010006.

Fields, G. S., 2003: Accounting for income inequality and its change: A new method, with application to the distribution of earnings in the United States. *Worker Well-Being and Public Policy*, Emerald Group Publishing Limited, 1–38, https://doi.org/10.1016/S0147-9121(03)22001-X.

Fornace, K. L., B. S. Whitney, V. Galy, K. A. Hughen, and F. E. Mayle, 2016: Late quaternary environmental change in the interior South American tropics: New insight from leaf wax stable isotopes. *Earth Planet. Sci. Lett.*, **438**, 75–85, https://doi.org/10.1016/j.epsl.2016.01.007.

Gan, M. A., V. B. Rao, and M. C. Moscati, 2005: South American monsoon indices. *Atmos. Sci. Lett.*, **6**, 219–223, https://doi.org/10.1002/asl.119.

Goswami, B. B., and B. N. Goswami, 2017: A road map for improving dry-bias in simulating the South Asian monsoon precipitation by climate models. *Climate Dyn.*, **49**, 2025–2034, https://doi.org/10.1007/s00382-016-3439-2.

He, C., and Coauthors, 2021a: Hydroclimate footprint of pan-Asian monsoon water isotope during the last deglaciation. *Sci. Adv.*, **7**, eabe2611, https://doi.org/10.1126/sciadv.abe2611.

——, Z. Liu, B. L. Otto-Bliesner, E. C. Brady, C. Zhu, R. Tomas, C. Buizert, and J. P. Severinghaus, 2021b: Abrupt Heinrich Stadial 1 cooling missing in Greenland oxygen isotopes. *Sci. Adv.*, **7**, eabh1007, https://doi.org/10.1126/sciadv.abh1007.

Hunke, E. C., 2010: Thickness sensitivities in the CICE sea ice model. *Ocean Modell.*, **34**, 137–149, https://doi.org/10.1016/j.ocemod.2010.05.004.

Hurrell, J. W., and Coauthors, 2013: The Community Earth System Model: A framework for collaborative research. *Bull. Amer. Meteor. Soc.*, **94**, 1339–1360, https://doi.org/10.1175/BAMS-D-12-00121.1.

Jackson, L. C., R. Kahana, T. Graham, M. A. Ringer, T. Woollings, J. V. Mecking, and R. A. Wood, 2015: Global and European climate impacts of a slowdown of the AMOC in a high resolution GCM. *Climate Dyn.*, **45**, 3299–3316, https://doi.org/10.1007/s00382-015-2540-2.

Jaeschke, A., C. Rühlemann, H. Arz, G. Heil, and G. Lohmann, 2007: Coupling of millennial-scale changes in sea surface temperature and precipitation off northeastern Brazil with high-latitude climate shifts during the last glacial period. *Paleoceanography*, **22**, PA4206, https://doi.org/10.1029/2006PA001391.

Kanner, L. C., S. J. Burns, H. Cheng, and R. L. Edwards, 2012: High-latitude forcing of the South American summer monsoon during the last glacial. *Science*, **335**, 570–573, https://doi.org/10.1126/science.1213397.

Lin, J. L., 2007: The double-ITCZ problem in IPCC AR4 coupled GCMs: Ocean–atmosphere feedback analysis. *J. Climate*, **20**, 4497–4525, https://doi.org/10.1175/JCLI4272.1.

Liu, X., and D. S. Battisti, 2015: The influence of orbital forcing of tropical insolation on the climate and isotopic composition of precipitation in South America. *J. Climate*, **28**, 4841–4862, https://doi.org/10.1175/JCLI-D-14-00639.1.

——, ——, R. H. White, and P. A. Baker, 2020: South American climate during the early Eocene: Impact of a narrower Atlantic and higher atmospheric CO_2. *J. Climate*, **33**, 691–706, https://doi.org/10.1175/JCLI-D-19-0170.1.

Liu, Z., and Coauthors, 2009: Transient simulation of last deglaciation with a new mechanism for Bølling-Allerød warming. *Science*, **325**, 310–314, https://doi.org/10.1126/science.1171041.

——, and Coauthors, 2014: Chinese cave records and East Asian summer monsoon. *Quat. Sci. Rev.*, **83**, 115–128, https://doi.org/10.1016/j.quascirev.2013.10.021.

Mayle, F. E., R. Burbridge, and T. J. Killeen, 2000: Millennial-scale dynamics of southern Amazonian rain forests. *Science*, **290**, 2291–2294, https://doi.org/10.1126/science.290.5500.2291.

Mohtadi, M., M. Prange, and S. Steinke, 2016: Palaeoclimatic insights into forcing and response of monsoon rainfall. *Nature*, **533**, 191–199, https://doi.org/10.1038/nature17450.

Mosblech, N. A., and Coauthors, 2012: North Atlantic forcing of Amazonian precipitation during the last ice age. *Nat. Geosci.*, **5**, 817–820, https://doi.org/10.1038/ngeo1588.

Neale, R. B., and Coauthors, 2010: Description of the NCAR Community Atmosphere Model (CAM 5.0). NCAR Tech. Note NCAR/TN-486+STR, 286 pp., https://www2.cesm.ucar.edu/models/cesm2/atmosphere/docs/description/cam5_desc.pdf.

Novello, V. F., and Coauthors, 2017: A high-resolution history of the South American monsoon from Last Glacial Maximum to the Holocene. *Sci. Rep.*, **7**, 44267, https://doi.org/10.1038/srep44267.

Nusbaumer, J., T. E. Wong, C. Bardeen, and D. Noone, 2017: Evaluating hydrological processes in the Community Atmosphere Model version 5 (CAM5) using stable isotope ratios of water. *J. Adv. Model. Earth Syst.*, **9**, 949–977, https://doi.org/10.1002/2016MS000839.

Oleson, K. W., and Coauthors, 2010: Technical description of version 4.0 of the Community Land Model (CLM). NCAR Tech. Note NCAR/TN-478+STR, 257 pp., https://doi.org/10.5065/D6FB50WZ.

O'Neil, J. R., R. N. Clayton, and T. K. Mayeda, 1989: Oxygen isotope fractionation in divalent metal carbonates. *J. Chem. Phys.*, **51**, 5547–5558, https://doi.org/10.1063/1.1671982.

Orrison, R., and Coauthors, 2022: South American monsoon variability over the last millennium in paleoclimate records and isotope-enabled climate models. *Climate Past*, **18**, 2045–2062, https://doi.org/10.5194/cp-18-2045-2022.

Peltier, W. R., D. F. Argus, and R. Drummond, 2015: Space geodesy constrains ice age terminal deglaciation: The global ICE-6G_C (VM5a) model. *J. Geophys. Res. Solid Earth*, **120**, 450–487, https://doi.org/10.1002/2014JB011176.

Samuels-Crow, K. E., J. Galewsky, D. R. Hardy, Z. D. Sharp, J. Worden, and C. Braun, 2014: Upwind convective influences on the isotopic composition of atmospheric water vapor over the Tropical Andes. *J. Geophys. Res. Atmos.*, **119**, 7051–7063, https://doi.org/10.1002/2014JD021487.

Smith, R., and Coauthors, 2010: The Parallel Ocean Program (POP) reference manual: Ocean component of the Community Climate System Model (CCSM) and Community Earth System Model (CESM). LAUR-10-01853, 141 pp., http://n2t.net/ark:/85065/d70g3j4h.

Strı́kis, N. M., and Coauthors, 2015: Timing and structure of mega-SACZ events during Heinrich Stadial 1. *Geophys. Res. Lett.*, **42**, 5477–5484A, https://doi.org/10.1002/2015GL064048.

——, and Coauthors, 2018: South American monsoon response to iceberg discharge in the North Atlantic. *Proc. Natl. Acad. Sci. USA*, **115**, 3788–3793, https://doi.org/10.1073/pnas.1717784115.

Tabor, C., and Coauthors, 2021: A mechanistic understanding of oxygen isotopic changes in the western United States at the Last Glacial Maximum. *Quat. Sci. Rev.*, **274**, 107255, https://doi.org/10.1016/j.quascirev.2021.107255.

Thompson, L. G., E. Mosley-Thompson, M. E. Davis, P.-N. Lin, K. A. Henderson, J. Cole-Dai, J. F. Bolzan, and K.-B. Liu, 1995: Late glacial stage and Holocene tropical ice core records from Huascaran, Peru. *Science*, **269**, 46–50, https://doi.org/10.1126/science.269.5220.46.

Vuille, M., R. S. Bradley, M. Werner, R. Healy, and F. Keimig, 2003a: Modeling δ^{18}O in precipitation over the tropical Americas: 1. Interannual variability and climatic controls. *J. Geophys. Res.*, **108**, 4174, https://doi.org/10.1029/2001JD002038.

——, ——, R. Healy, M. Werner, D. R. Hardy, L. G. Thompson, and F. Keimig, 2003b: Modeling δ18O in precipitation over the tropical Americas: 2. Simulation of the stable isotope signal in Andean ice cores. *J. Geophys. Res.*, **108**, 4175, https://doi.org/10.1029/2001JD002039.

Wang, X., A. S. Auler, R. L. Edwards, H. Cheng, E. Ito, Y. Wang, X. Kong, and M. Solheid, 2007: Millennial-scale precipitation changes in southern Brazil over the past 90,000 years. *Geophys. Res. Lett.*, **34**, L23701, https://doi.org/10.1029/2007GL031149.

——, and Coauthors, 2017: Hydroclimate changes across the Amazon lowlands over the past 45,000 years. *Nature*, **541**, 204–207, https://doi.org/10.1038/nature20787.

Zhang, Y., and Coauthors, 2015: Origin of increased terrigenous supply to the NE South American continental margin during Heinrich Stadial 1 and the Younger Dryas. *Earth Planet. Sci. Lett.*, **432**, 493–500, https://doi.org/10.1016/j.epsl.2015.09.054.

Zhou, J., and K. M. Lau, 1998: Does a monsoon climate exist over South America? *J. Climate*, **11**, 1020–1040, https://doi.org/10.1175/1520-0442(1998)011<1020:DAMCEO>2.0.CO;2.

Zhuravleva, A., M. Hüls, R. Tiedemann, and H. A. Bauch, 2021: A 125-ka record of northern South American precipitation and the role of high-to-low latitude teleconnections. *Quat. Sci. Rev.*, **270**, 107159, https://doi.org/10.1016/j.quascirev.2021.107159.

Zular, A., and Coauthors, 2019: The role of abrupt climate change in the formation of an open vegetation enclave in northern Amazonia during the late Quaternary. *Global Planet. Change*, **172**, 140–149, https://doi.org/10.1016/j.gloplacha.2018.09.006.